



NIH Public Access

Author Manuscript

J Am Chem Soc. Author manuscript; available in PMC 2014 November 20.

Published in final edited form as:

J Am Chem Soc. 2013 November 20; 135(46): 17417–17431. doi:10.1021/ja4078717.

L-edge X-ray Absorption Spectroscopy and DFT Calculations on Cu₂O₂ Species: Direct Electrophilic Aromatic Attack by Side-on Peroxo Bridged Dicopper(II) Complexes

Munzarin F. Qayyum[†], Ritimukta Sarangi[‡], Kiyoshi Fujisawa[¶], T. Daniel P. Stack[†], Kenneth D. Karlin[§], Keith O. Hodgson^{*†‡}, Britt Hedman^{*‡}, and Edward I. Solomon^{*†‡}

Department of Chemistry, Stanford University, Stanford, CA 94305, United States, Stanford Synchrotron Radiation Lightsource, SLAC, Stanford University, Menlo Park, CA 94025, United States, Department of Chemistry, College of Sciences, Ibaraki University, 2-1-1 Bunkyo, Mito, Ibaraki 310-8512, Japan, and Department of Chemistry, The Johns Hopkins University, Baltimore, MD 21218, United States

[†]Department of Chemistry, Stanford University, Stanford, CA 94305, United States

[‡]Stanford Synchrotron Radiation Lightsource, SLAC, Stanford University, Menlo Park, CA 94025, United States

[¶]Department of Chemistry, College of Sciences, Ibaraki University, 2-1-1 Bunkyo, Mito, Ibaraki 310-8512, Japan

[§]Department of Chemistry, The Johns Hopkins University, Baltimore, MD 21218, United States

Abstract

The hydroxylation of aromatic substrates catalyzed by coupled binuclear copper enzymes has been observed with side-on-peroxo-dicopper(II) (**P**) and bis- μ -oxo-dicopper(III) (**O**) model complexes. The substrate-bound-**O** intermediate in [Cu(II)₂(DBED)₂(O)₂]²⁺ (DBED=*N,N'*-di-*tert*-butyl-ethylenediamine) was shown to perform aromatic hydroxylation. For the [Cu(II)₂(NO₂-XYL)(O₂)]²⁺ complex, only a **P** species was spectroscopically observed. However, it was not clear whether this O-O bond cleaves to proceed through an **O**-type structure along the reaction coordinate for hydroxylation of the aromatic xylyl linker. Accurate evaluation of these reaction coordinates requires reasonable quantitative descriptions of the electronic structures of the **P** and **O** species. We have performed Cu L-edge XAS on two well-characterized **P** and **O** species to experimentally quantify the Cu 3d character in their ground state wavefunctions. The lower per-hole Cu character (40±6%) corresponding to higher covalency in the **O** species compared to the **P** species (52±4%) reflects a stronger bonding interaction of the bis- μ -oxo core with the Cu(III) centers. DFT calculations show that 10-20% Hartree-Fock (HF) mixing for **P** and ~38% for **O** species are required to reproduce the Cu-O bonding; for the **P** species this HF mixing is also required for an antiferromagnetically coupled description of the two Cu(II) centers. B3LYP (with 20% HF) was, therefore, used to calculate the hydroxylation reaction coordinate of **P** in [Cu(II)₂(NO₂-XYL)(O₂)]²⁺. These experimentally calibrated calculations indicate that the electrophilic attack on the aromatic ring does not involve formation of a Cu(III)₂(O²⁻)₂ species. Rather, there is direct electron donation from the aromatic ring into the peroxy σ^* orbital of the

*To whom correspondence should be addressed: hodgson@slac.stanford.edu; hedman@slac.stanford.edu; Edward.Solomon@stanford.edu.

SUPPORTING INFORMATION

Cu K-edge XAS spectra of **1** and **2**; details of the DFT-optimized geometric and electronic structures of **1** and **2**; key geometries and electronic structures along the reaction coordinates for [Cu(II)₂(NO₂-XYL)(O₂)]²⁺ (structures **A-L**) and [Cu(II)₂(NH₃)₄(O₂)]²⁺ (structures **X-Z**); full Gaussian 09 reference.

$\text{Cu(II)}_2(\text{O}_2^{2-})$ species, leading to concerted C-O bond formation with O-O bond cleavage. Thus, species **P** is capable of direct hydroxylation of aromatic substrates without the intermediacy of an **O**-type species.

1 INTRODUCTION

The coupled binuclear copper (CBC) proteins bind molecular oxygen (O_2) to form a side-on $\mu - \eta^2 : \eta^2$ peroxy dicopper(II) species (**P**) (Scheme 1, top).¹⁻⁶ The CBC proteins include hemocyanin (Hc), catechol oxidase (CO), tyrosinase (Ty) and NspF and are involved in a range of biological functions. Hemocyanin is the dioxygen transport protein in arthropods and mollusks. Tyrosinase and NspF⁷ catalyze the hydroxylation of phenols to *o*-diphenols (monooxygenation) along with the subsequent two-electron oxidation to the corresponding *o*-quinones (oxidoreduction) (Scheme 1, center). In addition, NspF can perform the oxygenation of *o*-aminophenols to nitrosophenols (hydroxyanilinase activity) (Scheme 1, bottom).⁷ In contrast, catechol oxidase performs only the oxidoreductase reaction. The side-on peroxy species (**P**) has been observed in all CBC enzymes. However, protein intermediates beyond **P** are unknown and the molecular mechanisms for the monooxygenation and oxidoreduction reactions remain unclear.

Synthetic models of the CBC active site have shown that Cu(I) can bind O_2 in several different modes.^{4,5,8-12} In particular, side-on peroxy Cu(II)_2 (**P**) and bis- μ -oxo Cu(III)_2 (**O**) species have been observed in different ligand systems (Scheme 2).^{4,5,8,13} The mode of O_2 binding depends on the nature of the ligand, its coordination geometry (including denticity and sterics)¹⁴ and the type of donor atom (i.e., aliphatic vs aromatic N-ligand, etc.),¹⁵ along with the solvent and counterion.^{4,8} In general, more sterically demanding, tridentate ligands favor the **P** species whereas strong σ donating, bidentate ligands that have limited steric interactions tend to stabilize the **O** isomer.^{4,5,16} The first X-ray crystal structure of a **P** species was solved by Kitajima and co-workers with a highly sterically hindered diisopropyl-substituted hydrotris(pyrazolyl)borate (TPB) ligand (Scheme 2, bottom left)^{17,18} that revealed a core almost identical to that of **P** found in CBC enzymes.^{19,20} Tolman and co-workers solved the crystal structure of the first **O** complex with a tridentate 1,4,7-tribenzyl-1,4,7-triazacyclononane (TACN^{Bn3}) ligand (Scheme 2, bottom center)^{21,22} and Stack and co-workers determined a bis- μ -oxo core in a bidentate *N,N'*-diethyl-*N,N'*-dimethyl-cyclohexylidiamine (L^{MECHD}) ligand system (Scheme 2, bottom right).²³

It has also been found that certain **P** complexes can be in rapid equilibrium with the **O** species. Stack and co-workers have demonstrated that the Cu(I) complex of a bidentate ligand, *N,N'*-di-*tert*-butyl-ethylenediamine (DBED), reacts with O_2 to form a mixture of **P**_{DBED} (~95%) and **O**_{DBED} (~5%) intermediates with the latter being the reactive oxidant in *o*-hydroxylation.^{24,25} Reaction of **P**_{DBED} with a phenolate substrate presumably requires axial phenolate binding to one Cu followed by a trigonal bipyramidal rearrangement of the phenolate into the equatorial Cu_2O_2 plane. This makes the phenolate a strong donor ligand that leads to O-O bond cleavage and formation of a bis- μ -oxo Cu(III)_2 -phenolate complex (Scheme 3). This is followed by C-O bond formation via an electrophilic aromatic substitution (EAS) mechanism. Thus, in the $[\text{Cu(II)}_2(\text{DBED})_2(\text{O}_2)]^{2+}$ model system, the **O** species is responsible for hydroxylation of the phenolate substrate.²⁵ In contrast to the above model system, Karlin and co-workers have demonstrated that the $[\text{Cu(I)}_2(\text{NO}_2\text{-XYL})]^{2+}$ complex reacts with O_2 to exclusively form a **P**_{NO₂-XYL} intermediate that is thought to directly hydroxylate the aromatic ring of the linker (Scheme 4).²⁶⁻²⁸

Due to the potential relevance of both the **P** and **O** species to the hydroxylation reaction performed by tyrosinase and NspF, it is important to gain quantitative experimental insight

into the electronic structures of these two systems. UV-Vis absorption and resonance Raman (rR) spectroscopic studies have demonstrated that the **P** and **O** species have distinct spectral features characteristic of their unique Cu₂O₂ cores (Scheme 2).^{17,23,29} X-ray absorption spectroscopy (XAS), which is a powerful element specific tool for electronic structure determination, was done at the Cu K-edge to reveal side-on peroxy species to be Cu(II) with a pre-edge transition at ~8979 eV, whereas bis- μ -oxo complexes have a pre-edge at ~8981 eV characteristic of Cu(III).³⁰ Both species, however, are EPR silent with no direct experimental quantification of the copper-dioxygen bonding interactions.

Here, for the first time, we have quantified directly the Cu-O bonding interaction in the **P** and **O** species using Cu L-edge XAS, which provides a sensitive probe of the charge on the copper ions and thus probes the covalent donor interactions of the peroxy and oxo ligands with the Cu centers. Two well-characterized systems, **P**^{TPB} (**1**) (Scheme 2, left) and **O**^{TEED} (**2**) (TEED = *N,N,N',N'*-tetraethylmethylenediamine, similar to the ligand in Scheme 2, bottom right), are used for the **P** and **O** species, respectively. The experimentally determined electronic structures of **1** and **2** are used to calibrate density functional theory (DFT) calculations to find the percent Hartree-Fock (HF) mixing required in a functional to quantitatively reproduce the covalent Cu-O bonding interactions. It is important to emphasize that DFT calculations with different amounts of HF mixing have been found to give quantitatively different descriptions of the bonding,^{31,32,33} and the determination of a meaningful reaction coordinate requires an accurate description of the electronic structure.

Using the experimentally calibrated DFT functional, we have investigated the hydroxylation mechanism in the [Cu(II)₂(NO₂-XYL)(O₂)]²⁺ system that is also a potential model for tyrosinase and NspF.^{26,34,35} This model complex is particularly interesting because it allows the study of the *o*-hydroxylation in a system where only the **P** species is present and the substrate does not bind to Cu, in contrast to the phenolate substrate-bonded **O** species in [Cu₂(DBED)₂(O₂)]²⁺. The goal is to determine whether the O-O cleaves along the reaction coordinate forming the **O** species before hydroxylation or whether the **P** intermediate is a viable candidate for hydroxylation in tyrosinase and NspF.

2 EXPERIMENTAL SECTION

2.1 Sample Preparation

The [{HB(3,5-*i*Pr₂pz)₃Cu}]₂(O₂), **1** (**P**^{TPB}), and [(L^{TEED}Cu)₂(O₂)]²⁺, **2** (**O**^{TEED}), complexes were prepared as described before.^{18,36} Both complexes are temperature sensitive and were handled under inert N₂ atmosphere and at dry ice temperatures during sample preparation.

2.2 L-edge X-ray Absorption Measurements and Data Analysis

For Cu L-edge XAS data collection, the solid samples were spread thinly over double-sided adhesive conducting graphite tape mounted on an Al sample paddle. The paddles were transferred onto a magnetic manipulator in an antechamber pre-chilled with liquid N₂ and then transferred into the main chamber and affixed to an Al block, which was cooled through conduction by a continuous flow of liquid He into a Cu block in an internal cavity. The temperature was monitored using a Lakeshore temperature controller and maintained at ~50 K during the course of data collection.

Cu L-edge X-ray absorption spectra were recorded at SSRL on the 31-pole wiggler beam line 10-1 under ring operating conditions of 50-100 mA and 3 GeV with a spherical grating monochromator with 1000 lines/mm and set at 30 μ m entrance and exit slits. Sample measurements were performed using the total electron yield mode, where the sample signal

(I_1) was collected with a Galileo 4716 channeltron electron multiplier aligned to 45° relative to the copper paddle. The signal was intensity-normalized (I_1/I_0) using the photocurrent of a gold grid reference monitor (I_0). Data for all samples were recorded in a sample chamber maintained below 10⁻⁶ Torr, isolated from the ultra-high vacuum beam line by a 1000 Å Al window.

External energy calibration was accomplished by L-edge measurements on CuF₂ before and after those of the sample. The L₃ and L₂ peak maxima were assigned to 930.5 and 950.5 eV, respectively. The variance in this calibration energy measured prior to and after each sample scan was used to shift linearly the experimental spectra between calibration scans. Spectra presented here are 3-5 scan averages, which were processed by fitting a second-order polynomial to the pre-edge region and subtracting it from the entire spectrum as background, resulting in a flat post-edge. The data were normalized to an edge jump of 1.0 at 1000 eV. The rising edges of the data were subtracted as arctangents. The total area under the L₃ and L₂ peaks was calculated by integrating the intensity between 925 and 955 eV. The integrated area was compared to that for D_{4h} [CuCl₄]²⁻ to obtain per-hole covalency numbers. Complex **2** decomposed to a Cu(II) species during data collection. The data for the pure decomposition Cu(II) product of **2** was also collected and subtracted from that of **2** to obtain the clean Cu(III) data. This led to a larger error of ±6% in **2** compared to ±4% in **1** for subsequent d-hole character determination.

2.3 K-edge X-ray Absorption Measurements and Data Analysis

The solid samples were ground in boron nitride at liquid N₂ temperature to form a homogeneous mixture that was pressed into a pellet and sealed between Kapton tape windows in a 1 mm aluminum spacer. The samples were maintained below 10 K during data collection using an Oxford Instruments CF 1208 continuous-flow liquid helium cryostat.

Cu K-edge X-ray absorption spectra were measured at SSRL on the unfocused 20-pole, 2.0-T wiggler beam line 7-3 under storage ring parameters of 50-100 mA and 3 GeV. A Rh-coated pre-monochromator, flat, bent mirror was used for harmonic rejection and vertical collimation. A Si(220) double crystal monochromator was used for energy selection. Transmission data were collected with N₂-gas-filled ionization detector (I_1). Internal energy calibration was accomplished by simultaneous measurement of the absorption of a Cu foil placed between two ionization chambers (I_1 and I_2) situated after the sample. The first inflection point of the foil spectrum was assigned to 8980.3 eV. The energy-calibrated transmission data (I_1/I_0) ($k = 13.4 \text{ \AA}^{-1}$) were processed by fitting a second-order polynomial to the pre-edge region and subtracting this from the entire spectrum as background. A one-region spline of order 2 was used to model the smoothly decaying post-edge region. Normalization of the data was achieved by scaling the spline function and data such that the value of the spline equals 1.0 at 9000 eV. This background subtraction and normalization was done using PySpline.^{37,38} Since some photodamage was observed over time, data presented in Figure S1 are the first scans of each data set to eliminate any spectral changes from photoreduction.

2.4 Computational Details

Spin-unrestricted broken-symmetry (BS) density functional theory (DFT) calculations were performed using the Gaussian 09³⁹ or ORCA 2.6.35⁴⁰ packages. Structures of **1** and **2** were calculated using the pure functional BP86 (Becke GGA exchange⁴¹ with Perdew 1986 nonlocal correlation⁴²) and the functional BLYP (Becke GGA exchange⁴¹ with Lee, Yang, and Parr correlation^{43,44}) modified to include 10, 20 and 38% Hartree-Fock.⁴⁵ The B3LYP hybrid functional (with 20% HF mixing)⁴⁶ was used to calculate the hydroxylation reaction coordinate, since it gives more accurate electronic structures than BP86, as determined in

Section 3.2.2. The TZVP basis set was used for the Cu, N and O atoms. The SVP basis set was used for B, C and H atoms. For the reaction coordinate analysis TZVP was also used for the *ortho*-C and *ortho*-H that participate in the hydroxylation reaction.

Geometry optimizations of **1** and **2** in vacuum were performed starting from crystallographically derived parameters¹⁸ where the modified crystal structure of $[(L^{MECHD}Cu)_2O_2]^{2+}$ ²³ (Scheme 2, bottom right) was used for **2**. The crystal structure of $[Cu(II)_2(H-XYL-O^-)(OH^-)]^{2+}$ ⁴⁷ was used to optimize the hydroxylated product $[Cu(II)_2(NO_2-XYL-O^-)(OH^-)]^{2+}$ with a *para*-NO₂ substituted xylol. The O···O unit (with O···O = 2.43 Å, Table S9) in the hydroxylated product was further modified into a peroxy (with O-O = 1.42 Å) and optimized to obtain the structure of the **P**^{NO₂-XYL} intermediate. The reaction coordinate for $[Cu(II)_2(NO_2-XYL)(O_2^{2-})]^{2+}$ was calculated from this starting structure of **P**^{NO₂-XYL}. The second reaction coordinate studied was for $[Cu(II)_2(NH_3)_4(O_2^{2-})]^{2+}$, where the starting side-on peroxy structure was optimized from the modified the crystal structure of **1**.

The self-consistent field (SCF) calculations were set to a tight convergence criterion. All fully optimized structures were verified as minima by frequency calculations that gave no imaginary frequency. The ν_{O-O} and ν_{C-O} obtained from the frequency calculations reported here were scaled by a factor of 0.965.^{48,49} Transition state (TS) structures were confirmed to have a single imaginary mode corresponding to the reaction coordinate. Intrinsic reaction coordinate (IRC) calculations showed that the TS structures are along the path between the reactants and products. Single point calculations on **P**^{NO₂-XYL} and the transition state structure were performed using the polarizable continuum model (PCM)⁵⁰ using the default parameters for CH₂Cl₂ (EPS = 8.93) to check for any effect on ΔG^\ddagger . Dispersion and relativistic effects were included using a VDW⁵¹ and DKH⁵² Hamiltonian where indicated in the text. QMForge⁵³ was used to calculate molecular orbital compositions via Mulliken population analysis⁵⁴ and for Mayer bond orders.^{55,56} Wave-functions were visualized and orbital contours were generated in VMD.⁵⁷ The two-dimensional potential energy surfaces were generated in gnuplot.

In agreement with the experimentally determined spin of **P** complexes, **P**^{NO₂-XYL} is well described by a broken-symmetry (BS) wave function with antiferromagnetically coupled Cu(II)'s, yielding a $M_S = 0$ ground state electronic structure. The BS energies of **P**^{NO₂-XYL} and structures along the reaction coordinate leading to the TS (with BS spin expectation, $\langle S^2 \rangle$, values of 0.7-1.0) were corrected for spin contamination from the triplet ($S_T = 1$) excited state to obtain the singlet ($S_T = 0$) energies using the spin corrected method by Yamaguchi et al. given by Equation 1:⁵⁸

$${}^1E = \frac{2^{BS}E - \langle S^2 \rangle_{BS}}{2 - \langle S^2 \rangle_{BS}} {}^3E \quad (1)$$

For the transition state structure and the ones that follow with BS $\langle S^2 \rangle$ values greater than 1.0, due to the formation of additional spins on the xylol ring and the distal oxygen, the BS energies are contaminated by the triplet ($S_T = 1$) and the quintet ($S_T = 2$) excited states. Equation 1 and 2⁵⁹ are used for spin correction for the $S_T = 1$ and $S_T = 2$ excited states, respectively:⁶⁰

$${}^1E = \frac{6^{BS}E - \langle S^2 \rangle_{BS}}{6 - \langle S^2 \rangle_{BS}} {}^5E \quad (2)$$

3 RESULTS AND ANALYSIS

3.1 L-edge X-ray Absorption Spectroscopy

The normalized, edge subtracted Cu L-pre-edge X-ray absorption spectra of $\{(\text{HB}(\text{3},\text{5}-i\text{Pr}_2\text{pz})_3\text{Cu})_2(\text{O}_2)\}$, **1** (**P^{TPB}**), and $[(\text{LEED}\text{Cu})_2(\text{O}_2)]^{2+}$, **2** (**O^{TEED}**), are presented in Figure 1 (left). The 2nd derivative of the expanded L₃ regions of the spectra of **1** and **2** are shown in Figure 1 (right). The Cu L-edge involves an electric dipole-allowed Cu 2p → 3d transition. The 2p⁵ core configuration of the final state undergoes spin-orbit coupling to give two peaks split by ~20 eV, the J = 3/2 L₃-edge at ~930 eV and the J = 1/2 L₂-edge at ~950 eV with an intensity ratio of ~2:1, respectively.⁶¹ The L₂-edge is ~1.5 times broader than the L₃-edge due to an additional Coster-Kronig Auger decay channel for this excited state.⁶² The L₃- and L₂-pre-edge features are followed by weak 2p → 4s and 2p → continuum edge transitions at ~10 eV higher energies (the intensity of the Δl = -1 transition is ~30 times lower than that of the Δl = +1 transition). The L₃-edge of **1** occurs at 931.0 eV, which is equivalent to the energy position of L₃ in D_{4h} [CuCl₄]²⁻ and comparable to L₃ transitions for many tetragonal Cu(II) complexes.⁶³ The L₃-edge of **2** is at 932.9 eV, shifted 1.9 eV to higher energy, consistent with a change in oxidation state to Cu(III).⁶⁴ An analogous trend in energy is observed for the L₂-edge.

The Cu 2p → 3d L-edge intensity can be used to experimentally obtain the amount of unoccupied metal d character in the ground state wavefunction and thus quantify the copper-dioxygen bonding. Since the Cu 2p orbital is localized on the Cu center and the 2p → 3d transition is electric dipole-allowed, the total intensity of the L₃- and L₂-pre-edges reflects the Cu d character in the Ψ_{LUMO}^* . The oxygen and nitrogen ligand valence 2p orbitals undergo bonding/antibonding interactions with the Cu 3d orbitals leading to the mixing of some ligand 2p character (β^2) into the ground state wavefunction.⁶⁵ Thus, increasing ligand character (covalency) in the ground state decreases the metal 3d character and therefore the intensity of the 2p → 3d Ψ_{LUMO}^* transition by β^2 (Equation 3).

$$\Psi_{\text{LUMO}}^* = \sqrt{1 - \beta^2} |\text{Cu}(3d_{x^2-y^2})\rangle - \beta |\text{Ligand(np)}\rangle \quad (3)$$

Correlating the L-edge intensity of **1** and **2** with that of the well characterized D_{4h} [CuCl₄]²⁻ complex ($61 \pm 4\%$ Cu d character in the $\Psi_{\beta-\text{LUMO}}^*$) gives a quantitative estimate of the amount of Cu unoccupied 3d character in their ground state wavefunctions. Table 1 lists the Cu characters obtained from the total integrated intensity of the L-edge spectra of **1** and **2**.⁶⁶ Accounting for two 3d holes per Cu for **2** and one hole for **1** and D_{4h} [CuCl₄]²⁻, the unoccupied Cu character of **1** and **2** are $52 \pm 4\%$ and $40 \pm 6\%$, respectively. The decrease in Cu d character in **1** and **2** compared to that in D_{4h} [CuCl₄]²⁻ indicates stronger covalent mixing of the Cu centers with the ligand (predominantly oxygen) valence orbitals. Furthermore, the higher covalency of **2** relative to **1**, indicates that the Cu centers in the **O^{TEED}** species have a stronger bonding interaction with the oxygen bridging ligands than in the **P^{TPB}** species, consistent with shorter Cu(III)-O bonds in the **O^{TEED}** complex (~1.80 Å versus ~1.90 Å).

3.2 Calculations

3.2.1 Geometric Structure—It has been established that the amount of Hartree-Fock (HF) mixing in DFT functionals affects calculated geometric and electronic structures.^{31,32,67,68} Therefore, we have performed DFT calculations with varying HF mixings to determine the amount that best reproduces geometric and electronic structures of

1 and **2**. Specifically, we have used the pure functional BP86 and BLYP modified with 10%, 20% (B3LYP), and 38% HF mixing to calculate the structures of **1** (Figure 2, left) and **2** (Figure 2, right). Selected structural parameters from the DFT-optimized structures of the two complexes are compared to those obtained from crystallography in Tables 2, 3, S1 and S2. The crystal structure of **1** is available,¹⁸ whereas no crystal structure of **2** exists; $[(L^{MECHD}Cu)_2O_2]^{2+}$ (Scheme 2, bottom right) most closely resembles complex **2** and was used for comparison.²³

In the case of complex **1**, the experimental planar Cu₂O₂ core is better reproduced with Hartree–Fock mixing. With BP86, the Cu₂O₂ core is butterfly by 5.4° (Table 2 $\angle Cu1,O3,O4,Cu2$) while inclusion of 10% HF gives a planar structure. The calculated Cu···Cu and O–O distances along the series with increasing HF are characteristic of **P** complexes but are slightly longer than the crystallographic distances (variations in Cu···Cu and O–O along the series are within 0.17 Å and 0.07 Å, respectively, of the X-ray parameters). A similar variation in the DFT optimized bond lengths of **P** species has been observed before.¹⁵ Based only on these structural parameters there is no significant advantage of any functional.

The calculated structures of **2** show a planar Cu₂O₂ core paralleling the crystal structure of $[(L^{MECHD}Cu)_2O_2]^{2+}$. The cores are planar for all **O** species studied to date (Table S3).^{21-23,36,69-74} A slight improvement in the bond lengths of the Cu₂O₂ core (Cu···Cu, O···O, and Cu–O) is observed with 20–38% Hartree–Fock mixing. The experimental and calculated difference in the Cu···Cu and O···O distances along the series of differing HF mixing are within 0.05 Å and 0.03 Å, respectively, and smaller than the difference observed for the **P** complexes. All the other calculated distances of **2** are in reasonable agreement with the crystal structure of $[(L^{MECHD}Cu)_2O_2]^{2+}$ (within ~0.08 Å). Again, there is no significant dependence of the geometric structure on the choice of functional.

3.2.2 Electronic Structure—For coupled binuclear Cu(II)₂ systems, the half-occupied d orbitals on the two Cu_(1,2) centers form symmetric ($d_1 + d_2$) and antisymmetric ($d_1 - d_2$) combinations. In O₂²⁻, the degenerate π^* orbitals are occupied (HOMOs), while the σ^* is unoccupied (LUMO) (Figure 3, right). When O₂²⁻ binds to Cu in **1**, the π^* splits into π_{σ}^* (orbital in the Cu₂O₂ plane) and π_{ν}^* (orbital out of the Cu₂O₂ plane). The π_{σ}^* undergoes σ bonding and antibonding interactions with the symmetric combination of Cu d_{x²-y²} orbitals to form the HOMO-2 O₂²⁻ $\pi_{\sigma}^* \alpha + 2Cu^{2+}$ (d_{x²-y²} + d_{x²-y²}) and the LUMO [2Cu²⁺ (d_{x²-y²} + d_{x²-y²}) – O₂²⁻ $\pi_{\sigma}^* \alpha$], respectively (Figure 3, center and Figure 4, left). The peroxy σ^* similarly forms a bonding and antibonding pair with the antisymmetric combination of filled Cu d_{x²-y²} orbitals to form the HOMO [2Cu²⁺ (d_{x²-y²} – d_{x²-y²} + O₂²⁻ σ^*)] and the LUMO+1 [O₂²⁻ σ^* – 2Cu²⁺ (d_{x²-y²} – d_{x²-y²})], respectively (Figure 3, center and Figure 4, left). The LUMO+1 peroxy σ^* is ~3–6 eV higher in energy than the Cu based LUMO. There is a small amount of backbonding from the occupied Cu d orbitals into the σ^* orbital that results in some σ^* character in the HOMO (Figure 4).

As HF mixing is increased, the calculated electronic structure of **1** shows decreasing amounts of σ donation from the filled O₂²⁻ π_{σ}^* into the symmetric 2Cu (d_{x²-y²} + d_{x²-y²}) LUMO (Table S4). The resulting Cu d-hole character for the different functionals is given in Table 4. The closest match to the experimental covalency for **1** (52 ± 4% unoccupied Cu character) is obtained with 10–20% HF (49–57% Cu character). The addition of a HF contribution to the functional also leads to spin polarization of the α and β LUMOs as reflected by the increasing spin expectation value (Table 4) consistent with a Broken Symmetry ($M_S = 0$) singlet ground state. The spin polarized α and β holes reside in the 3d_{x²-y²} orbitals on each Cu and undergo covalent mixing with the peroxy π_{σ}^* orbital (Figure

5, left). Spin polarization is not observed with the pure functional (BP86) where both the α and β holes are delocalized over both Cu's and the amount of d-hole per Cu is underestimated (45% Cu character) indicating that this functional is too covalent (Figure 5, right). Thus, some HF mixing (10-20%) is required to reproduce the experimental covalency of **1**, which results in spin polarization of the Cu(II)'s consistent with the antiferromagnetically coupled description of **1**.

When **P** isomerizes to **O**, the O–O bond is cleaved. This lowers the peroxy σ^* in energy, oxidizes the Cu(II) to Cu(III) and reduces the O_2^{2-} to O^{2-} leading to complex **2**.⁷⁵ This results in two Cu based LUMO's that are the symmetric and antisymmetric combinations of the Cu $d_{x^2-y^2}$ orbitals and are antibonding with the oxo in-plane 2p orbitals (Figure 4, right). These LUMO and LUMO+1 are separated by <0.2 eV such that both contribute to the single L pre-edge feature in Figure 1. Note that in the **P** complex, the σ^* is ~3-6 eV higher in energy with little Cu character and does not contribute to the pre-edge.

The calculated electronic structure of **2** shows increasing amounts of Cu d character in the LUMO and LUMO+1 as % HF mixing is increased (Table S5). Table 4 summarizes the total d-hole character per Cu for the different functionals using Mülliken populations. The closest match to the experimental covalency for **2** ($79 \pm 6\%$ Cu hole) is obtained with 38% HF (77% Cu hole). Both the LUMO and LUMO+1 are delocalized and highly covalent with 36.4% and 40.4% Cu character, respectively (Figure 6).

Thus, HF mixing is required to reproduce the experimentally observed electronic structures of both **P** and **O** species. The closest agreement with the experimental covalency of **1** is with 10-20% HF, whereas ~38% HF best reproduces that of **2**. We have, therefore, selected B3LYP (with 20% HF) to study the electrophilic aromatic substitution (EAS) reaction coordinate in the $[Cu(II)_2(NO_2-XYL)(O_2)]^{2+}$ complex to determine the point of O–O bond cleavage with respect to the transition state. To this end, the reaction coordinate obtained for the **PNO₂-XYL** structure will be compared with that of the **O^{DBED}** complex studied previously with the B3LYP functional as well.^{24,25}

3.3 Reaction Coordinate

3.3.1 PNO₂-XYL Intermediate and Hydroxylated Product—In order to evaluate the EAS reaction coordinate of $[Cu(II)_2(NO_2-XYL)(O_2)]^{2+}$, we first obtained the geometry optimized structures of the **PNO₂-XYL** reactant and the hydroxylated product $[Cu(II)_2(NO_2-XYL-O^-)(OH^-)]^{2+}$. The calculated ν_{0-0} for **PNO₂-XYL** (Figure 7A) is 879 cm^{-1} (the experimental ν_{0-0} is 747 cm^{-1})^{28, 76, 77} and described with a BS singlet ($M_S = 0$) ground state with spin polarized α (2% Cu₁ and 48% Cu₂ in the LUMO) and β holes (48% Cu₁ and 2% Cu₂ in the LUMO) in the $3d_{x^2-y^2}$ orbital on each Cu (Table S6). The total Cu character is consistent with Cu L-edge XAS data for **1** (Table 1). Selected structural parameters are given in Table S8 (**PNO₂-XYL**). The Cu₂O₂ core is butterflied to 138° to accommodate the xylyl bridge and is consistent with the split $O_2^{2-}\pi_\sigma^*$ charge transfer transitions (360 nm and 435 nm) from absorption studies.^{28,77} The Cu–Cu and O–O distances are 3.57 Å and 1.42 Å, respectively, while the average Cu–O bond length is 2.04 Å. These distances are characteristic of **P** species.¹⁵ The distance between the proximal oxygen (O₃) and the nearest *ortho*-carbon of the arene (C₁₂) is 2.79 Å. Based on this unconstrained structure, the C–O and O–O distances of 2.80 Å and 1.42 Å, respectively, were used as the starting point for a scan of the two-dimensional reaction coordinate presented in Section 3.3.2.

The final hydroxylated product $[Cu(II)_2(NO_2-XYL-O^-)(OH^-)]^{2+}$ formed in the EAS reaction (Figure 7B) (see Section 3.3.3) has the O–O bond cleaved with a calculated distance of 2.43 Å (crystallographic O–O = 2.43 Å⁴⁷).⁷⁸ The C–O bond is fully formed at

1.33 Å (crystallographic C–O = 1.33 Å) and the phenolate product bridges the two Cu(II) centers. All other calculated structural parameters compare well with the crystal structure (Table S9). The Cu₂O₂ core and the resulting phenolate are nearly planar ($\angle \text{CuOOCu} = 177^\circ$ calc, 178° x-ray; $\angle \text{C}_{15}\text{C}_{12}\text{O}_3 = 180^\circ$ calc, 178° x-ray). The experimental $\nu_{\text{C}-\text{O}}$ of 1320 cm⁻¹ is in good agreement with the calculated frequency of 1302 cm⁻¹.²⁸ Formation of this hydroxylated product will be discussed in Section 3.3.3.

3.3.2 2-D Reaction Coordinate of O–O Bond Cleavage and C–O Bond

Formation—Reaction of the P^{NO₂–XYL} intermediate (Figure 7A) to form the hydroxylated product [Cu(II)₂(NO₂–XYL–O⁻)(OH⁻)]²⁺ (Figure 7B), requires cleavage of the O₃–O₄ and C₁₂–H₁₁ bonds and formation of the C₁₂–O₃ and O₄–H₁₁ bonds. In Section 3.3.3, it is shown that the cleavage of the C₁₂–H₁₁ bond (and the subsequent formation of the O₄–H₁₁ bond) occurs after the transition state for C₁₂–O₃ formation, consistent with the experimental kinetic isotope effect of ~1.0. In this section, the cleavage of the O₃–O₄ and formation of the C₁₂–O₃ bonds are evaluated. The two-dimensional potential energy surface (PES) of the electronic energy as a function of the O₃–O₄ and C₁₂–O₃ distances is presented in Figure 8. The C₁₂–O₃ was decreased in steps of 0.20 Å from 2.80 Å to 1.60 Å and for every point the O₃–O₄ bond was elongated (1.45, 1.60, 1.80, 2.10, and 2.28 Å). This 2-D PES compares the energetics of the two possible reaction pathways: i) concerted reaction where the C₁₂–O₃ forms concurrently with O₃–O₄ cleavage (pink curve in Figure 8) and ii) step-wise reaction where the C₁₂–O₃ forms after complete O₃–O₄ cleavage (green curve in Figure 8). Figure 8 shows that the concerted reaction is energetically favorable and gives the lowest energy route on the PES (pink curve). The alternate route of first forming O^{NO₂–XYL} (followed by C₁₂–O₃ bond formation) (green curve) is higher in energy by ~20 kcal/mol. The lowest energy route (pink line) is re-plotted in Figure 9, top, with additional points added near the transition state (TS) and at the end point K (the unconstrained species with C₁₂–H₁₁ still present) with a C₁₂–O₃ of 1.41 Å.

TS Geometric and Electronic Structure: The transition state along the C₁₂–O₃ bond formation reaction coordinate occurs at a C₁₂–O₃ distance of 1.88 Å (G) (Figure 9, top). This has one imaginary frequency of -547 cm⁻¹ (with a displacement ratio of 0.63 O₃ : -0.25 O₄ : -0.48 C₁₂ : 0.44 H₁₁) (Figure 9, bottom, magenta arrow) showing O₃–O₄ bond cleavage occurs concurrently with C₁₂–O₃ bond formation. The calculated energy barriers, ΔH and ΔG, corrected for spin contamination, are ~24 kcal/mol and ~26 kcal/mol, respectively. When dispersion and relativistic effects are also included,^{79,80} the barrier height is lowered by ~5 kcal/mol and within DFT accuracy of the experimental activation energies (experimental $\Delta H^\ddagger = 13 \pm 2$ kcal/mol, $\Delta G^\ddagger = 15 \pm 2$ kcal/mol).^{28,81,82} An intrinsic reaction coordinate (IRC) calculation confirms that the TS is along the EAS reaction coordinate.

In going from point A to the TS structure (G), the O₃–O₄ distance increases from 1.42 Å to 1.97 Å while the Cu₁–Cu₂ distance decreases from 3.57 Å to 3.29 Å (Table S8). A decrease in the Cu–O distances is also observed (Cu–O_{ave} is 2.04 Å at point A and 1.94 Å at point G, Table S8). The key angles to note are the $\angle \text{Cu}_1\text{O}_3\text{O}_4\text{Cu}_2$ dihedral angle of the Cu₂O₂ core that becomes more planar (138° at point A and 159° at point G) and the phenolate angle ($\angle \text{C}_{15}\text{C}_{12}\text{O}_3$) that becomes more perpendicular (122° at point A and 113° at point G). Another important geometric change observed at the TS is distortion of C₁₂ of the xylyl ring from a planar sp² to a pseudo tetrahedral sp³ hybridized state ($\angle \text{C}_{15}\text{C}_{12}\text{H}_{11}$ is 177° at point A and 158° at point G). The C₁₂–H₁₁ bond distance decreases consistently from 1.079 Å at point A ($\nu_{(\text{C}-\text{H})} = 3209$ cm⁻¹) to 1.075 Å (at point D) before the TS and at the TS it increases slightly to 1.080 Å ($\nu_{(\text{C}-\text{H})} = 3195$ cm⁻¹) and continues to increase (Table S8).

The kinetic isotope effect (KIE) is calculated to be 1.00, which matches the experimentally observed KIE of ~1.0.^{83,27}

Changes in the electronic structure from point **A** to **G** were investigated by monitoring the Mayer bond order (MBO) (Table 5) that show that as the C₁₂–O₃ bond is strengthened, the O₃–O₄ bond is weakened. To obtain a reference for a full C–O bond, structure **K** was reoptimized with the C₁₂–H₁₁ proton removed (structure **L**, C₁₂–O₃ MBO of 1.180) (Table 5).⁸⁴ The O–O MBO of structure **A** (0.733) is used as the reference for an unperturbed side-on peroxy O–O bond. Thus, at the TS, the C₁₂–O₃ is found to be 25% formed while 63% of the O–O bond is broken (the TS of the EAS reaction for [(DBED)₂Cu(III)₂(O²⁻)₂]²⁺ had 27% of the C–O bond formed while the O···O bond was fully broken²⁵).

Inspection of the Mulliken charge and spin densities on the different fragments (Cu₁, Cu₂, O₃, O₄, xylyl-ring (NO₂–C₆H₃), and rest of the ligand) provides insight into the electronic structure changes that occur along the reaction coordinate (Tables 6, 7, S10 and S11). The two Cu centers remain spin polarized and antiferromagnetically coupled from points **A** to **G** (+0.52 spin on Cu₁ and -0.52 spin on Cu₂ at point **G**, Table 7) and thus are described as Cu(II) centers.⁸⁵ It is important to note that the xylyl ring becomes noticeably positive with the Mulliken charge increasing from +0.02 at point **A** to +0.25 at point **G** (Table 6, combined charge on fragments (NO₂–C₆H₂) and H₁₁). In addition, at point **G** there is a net β spin of -0.29 on the xylyl ring whereas the net spin at point **A** is 0.00 (Table 7, combined spin on fragments (NO₂–C₆H₂) and H₁₁). This increase in positive Mulliken charge and β spin on the xylyl ring is due to a 23% α electron donation from the π electron cloud of the xylyl ring (Table 8) (Figure 10, orbital 188 α in **A**) into the O₂²⁻ σ^* orbital (Figure 10, orbital 210 α in **A**)⁸⁶ forming orbital 197 α at point **G** (Figure 10). Thus, at the TS, the O₃–O₄ weakens due to α electron donation from the xylyl ring. As the peroxide elongates and starts to cleave, the holes on the O₂²⁻ σ^* orbital are spin polarized leading to a partial β hole on the distal O₄ (+0.52 α spin) and a partial α hole on the proximal O₃ (-0.21 β spin) (Table 7). The α hole on the O₃ is smaller than the β hole on the distal O₄ because of the α electron donation from the xylyl ring to O₃. Thus, at the TS the C₁₂–O₃ bond is strengthened while the O₃–O₄ bond is weakened in a concerted manner due to the transfer of partial α electron density from the ring into the O₃–O₄ bond.

Species K: From the TS to the end of the reaction before H₁₁ is lost as a proton, the optimized C₁₂–O₃ decreases from 1.88 Å at point **G** to 1.41 Å at point **K**. The O₃–O₄ distance increases from 1.97 Å to 2.49 Å from point **G** to **K** while the C₁₂–H₁₁ has elongated from 1.08 Å in **G** to 1.12 Å in **K** (Table S8). The Cu₂O₂ core becomes mostly planar with the \angle Cu₁O₃O₄Cu₂ dihedral angle increasing from 159° at point **G** to 174° at point **K**. In addition, the phenolate angle (\angle C₁₅C₁₂O₃ in Figure 11) increases from 113° at point **G** to 145° at point **K** (Table S8) but is still not planar. This bent phenolate angle has an important role that will be explored below.

Inspection of the electronic structure at point **K** reveals that the two Cu centers continue to be spin polarized (+0.59 spin on Cu₁ and -0.57 spin on Cu₂, Table 7) with no increase in Mulliken charge (Table 6) and thus remain antiferromagnetically coupled Cu(II) centers. The β spin character on the xylyl ring has increased to -0.98 while the α spin character on the distal O₄ has increased to +0.96 (Table 7). The increase in β spin density on the xylyl ring is due to an additional 31% α electron donation (Table 8) from the ring to the O₃–O₄ from point **G** to **K**, leaving an α hole in a phenolate-like orbital on the ring (Figure 10 K, orbital 198 α and a β spin character of -0.98). The increase of α spin character on the distal O₄ is a result of the complete cleavage of the O₃–O₄ bond that leads to full spin polarization of the O···O σ^* with the α and β holes localized on O₃ and O₄, respectively. Another important change in the electronic structure at point **K** is that the overall Mulliken charge on

the xylyl ring has decreased from 0.25 at the TS to 0.18 (Table 6). This decrease in charge on the ring is due to β electron donation from O₃ to form the C₁₂–O₃ bond with 38% of the electron density residing on the xylyl ring (Table 8). Thus, the α and β electrons from the xylyl ring and O₃, respectively, pair for the concerted C₁₂–O₃ bond formation with O₃–O₄ bond cleavage. However, only 76% of the C₁₂–O₃ is formed with the O₃–O₄ completely broken (Table 5) as the C₁₂–H₁₁ bond is still present. The C₁₂–H₁₁ bond cleavage is explored in Section 3.3.3.

1 Versus 2 Electron Donation from Substrate: At the end of the above reaction coordinate at point **K**, a partial α electron has been transferred from the xylyl ring to the O···O forming an antiferromagnetically coupled diradical pair with a β spin on the xylyl ring (substrate) and an α spin on the distal O₄. Interestingly, when an unconstrained benzene was used as the substrate for this reaction using a side-on peroxy [Cu(II)₂(NH₃)₄(O₂²⁻)]²⁺ structure as a model (species **X** in Figure 12, Table S13), the species formed at the end of the reaction and before C-H bond cleavage, had no diradical character on the substrate and distal O₄ (species **Z** with a C-O distance of 1.36 Å in Figure 12, Table S13 and S15). Evaluation of the reaction coordinate for [Cu(II)₂(NH₃)₄(O₂²⁻)]²⁺ reveals that the side-on peroxy species **X** does react with the substrate to proceed through a transition state, **Y**, with a small amount of diradical character on the aromatic substrate (spin of +0.23) and the distal O₄ (spin of -0.19) (Table S15) and a phenolate angle, \angle CCO, of 119° (Table S13, point **Y** with a C-O distance of 2.08 Å).⁸⁷ The diradical character, however, disappears farther along the reaction as the substrate rotates (\angle CCO = 163° at point **Z**, Figure 13, right) to allow the second π electron of the HOMO orbital on the ring to overlap the peroxy based LUMO leading to α , β electron pair donation from the substrate.⁸⁸ Thus, the only spins observed are the two antiferromagnetically coupled Cu centers (+0.53 on Cu₁ and -0.54 on Cu₂, Table S15) that remain Cu(II) throughout the reaction coordinate.⁸⁹ If at point **Z** (Figure 12) the benzene ring is constrained with respect to the Cu₂O₂ plane to a \angle CCO of 145°, consistent with the covalently linked xylyl ring of [Cu(II)₂(NO₂-XYL)(O₂)]²⁺ at point **K** (Figure 13, left), the species does contain diradical character. Upon removing the constraint on the ring in this spin polarized complex, the ring rotates by ~20° allowing a second electron to transfer and eliminate the diradical character.⁹⁰

3.3.3 C₁₂–H₁₁ Cleavage and Completion of the Reaction—In order to fully form the hydroxylated product [Cu(II)₂(NO₂-XYL-O⁻)(OH⁻)]²⁺, the C₁₂–H₁₁ proton was removed and the distal O₄ protonated. However, due to the large distance between H₁₁ and O₄, an exogenous proton acceptor is potentially needed to facilitate this transfer. In these calculations, methylamine is used as a model for this exogenous base.⁹¹ Op't Holt et al. showed that the use of stronger/weaker proton acceptors did not significantly change the reaction coordinate.²⁵ The effect of the C₁₂–H₁₁ bond cleavage was modeled with a 2D PES by adding methylamine to the nine structures from C to K in Figure 9 (C₁₂-Nmethylamine constrained to 2.80 Å) with the lone pair on the N pointing towards the *ortho*-H₁₁. For each of the nine structures, the N-H₁₁ distance was scanned from 2.06, 1.80, 1.60, 1.40, 1.20 to 1.03 Å, resulting in cleavage of the C₁₂–H₁₁ bond. The 2-D PES of the electronic energy calculated as a function of the C₁₂–O₃ and N_{base}–H₁₁ bond distances is shown in Figure 14. The electronic energy is scaled relative to that of **A_b** (C₁₂–O₃ = 2.80 Å; C₁₂–H₁₁ = 1.08 Å), which has the same structure as **A** in Figure 9 but with base present (base is also present in structures **C_b**, **K_b** and **L_b**). The lowest energy path (red line) from **C_b** (C₁₂–O₃ = 2.40 Å; C₁₂–H₁₁ = 1.08 Å) to **K_b** (C₁₂–O₃ = 1.41 Å; C₁₂–H₁₁ = 1.12 Å) has essentially the same geometric and electronic structures as those without base present in Figure 9. Thus, the TS state remains unchanged in the presence of a base.

When the C₁₂–O₃ bond is constricted sufficiently to 1.41 Å (**K_b**), it becomes energetically favorable for the proton to be transferred to the nearby base forming structure **L_b** (C₁₂–O₃ = 1.32 Å; C₁₂–H₁₁ = 1.73 Å), which is ~41 kcal/mol lower in energy than **A_b**. Along the reaction coordinate from **K_b** to **L_b** (Tables S16–18), the diradical character on the xylyl ring and distal O₄ disappears as the C₁₂–H₁₁ bond is elongated from 1.12 Å to 1.25 Å and the ∠CCO becomes more planar (Table S18). This reflects the additional transfer of the second electron from the xylyl ring (Figure 10 **K**, orbital 196β) to the hole on the distal O₄ (Figure 10 **K**, orbital 197β). Further C₁₂–H₁₁ bond elongation to 1.73 Å in **L_b** completes C₁₂–O₃ bond formation (MBO of 1.18).

Finally, transfer of a proton from the base to the distal O₃, gives another ~40 kcal/mol energy stabilization. Thus, formation of the hydroxylated species [Cu(II)₂(NO₂-XYL-O⁻)(OH⁻)]²⁺ via a base is energetically favorable. The hydroxylated species formed has a structure that is very similar to that of **L_b**. Protonation of the distal O, therefore, has no substantial effect on the Cu₂O₂ core.

4 DISCUSSION

L-edge XAS experimentally quantified the amount of Cu character in the ground state wavefunction (Cu 3d character in the unoccupied orbitals) to be 52 ± 4% in **1** (**P**^{TPB}) and 79 ± 6% in **2** (**O**^{TEED}). The 52% Cu character in **1** corresponds to one hole per Cu(II) center, whereas, the 79% Cu character in **2** corresponds to two holes per Cu(III) center. The lower per-hole Cu character and thus higher covalency in **2** compared to **1**, indicates that the bis-μ-oxo core has a stronger bonding interaction with the Cu centers. The results from L-edge XAS have been correlated to DFT calculations to determine that a HF mixed hybrid functional is required to reproduce the quantitative electronic structures of **1** and **2**. In addition to increasing the Cu 3d-hole character, inclusion of HF mixing leads to spin polarization in **1** with each hole localized on a different Cu. Thus, HF mixing is required to produce the singlet ground state with an antiferromagnetically coupled pair of Cu(II) centers (Figure 5).

B3LYP (with 20% HF), which gives a reasonable comparison to the L-edge XAS data for **1** and **2** was then employed to evaluate the EAS reaction coordinate in [Cu(II)₂(NO₂-XYL)(O₂)]²⁺ that has an experimentally defined **P** intermediate. Stack and co-workers have previously shown that the **O** isomer in [(DBED)₂Cu₂(O₂)]²⁺, another potential tyrosinase model, is capable of performing aromatic hydroxylation.^{24,25} The goal here was to determine whether the **P**^{NO₂-XYL} in [Cu(II)₂(NO₂-XYL)(O₂)]²⁺ converts to an **O**^{NO₂-XYL} intermediate along the reaction coordinate for EAS. This is an ideal system to study because the substrate does not bind to the Cu, in contrast with the [(DBED)₂Cu(III)₂(O₂)]²⁺ system, where the phenolic substrate binds to one of the Cu centers and then undergoes EAS. Two key differences are observed in comparing the reaction coordinate of [Cu(II)₂(NO₂-XYL)(O₂)]²⁺ to the previously developed model of [(DBED)₂Cu(III)₂(O₂)]²⁺. First, the calculations show that for [Cu(II)₂(NO₂-XYL)(O₂)]²⁺, the Cu centers remain antiferromagnetically coupled Cu(II) throughout the reaction and are not oxidized to Cu(III). The aromatic ring of the crosslinker transfers π electron density directly to the peroxy σ^* orbital resulting in O–O bond cleavage with concerted C–O bond formation (Scheme 5). Thus, the **P** intermediate is best interpreted to be the reactive species in [Cu(II)₂(NO₂-XYL)(O₂)]²⁺ that performs the EAS reaction.

Second, instead of transferring a pair of electrons from the aromatic ring in [Cu(II)₂(NO₂-XYL)(O₂)]²⁺ to form the C–O bond, α and β electrons are transferred from the xylyl ring and the peroxy π^* , respectively, due to the limited flexibility of the xylyl chelate (Figure 15). The α counterpart of the peroxy π^* ends up on the distal oxygen (O_d) resulting in a radical

on the ring and a radical on O_d that are antiferromagnetically aligned. This diradical character is eliminated as the *o*-C-H cleaves and a second electron is transferred from the ring to O_d via the O_p-Cu-O_d bonding network. This one versus two electron attack is due to the \angle CCO phenolate angle (Figure 13). In [Cu(II)₂(NO₂-XYL)(O₂)]²⁺, where the rotation of the aromatic ring is constrained by covalent linkage to be less than 145°, only one electron transfer to peroxide is observed. As the \angle CCO becomes more planar with weakening of the *o*-C-H bond, the second electron is transferred. In contrast, in the EAS reaction coordinate where the aromatic ring is allowed to freely rotate (Figure 13), the \angle CCO becomes >163° and a two electron attack is observed as found for **O** in [(DBED)₂Cu₂(O₂)]²⁺.²⁵

Thus, both the **P** and **O** species are capable of performing aromatic hydroxylation via their separate mechanisms. The question now in tyrosinase and NspF is whether **P** is the reactive species or converts to **O** upon phenolic substrate binding. The strength of the substrate-Cu interaction in the enzyme will be a key determining factor. While no substrate-bound oxy-CBC intermediate has been characterized spectroscopically, inhibitor binding studies have shown that substrate analogs bind to the Cu(II) in tyrosinase.^{92,93} These studies also show that the interaction of the substrate with the protein pocket influences this binding. Thus, the combined influence of the Cu and protein pocket interactions will determine the nature of the Cu₂O₂ species; the stronger and more equatorial the substrate binding, the more favorable the conversion of **P** to **O**. These combined interactions will also determine the orientation of the substrate and whether the transfer of the electron pair is concerted during this electrophilic reaction.

Supplementary Material

Refer to Web version on PubMed Central for supplementary material.

Acknowledgments

We are grateful to the National Institutes of Health (NIH) (E.I.S., DK31450; K.O.H., P41 RR001209 and GM103393; K.D.K., GM28962) and the Japan Society for the Promotion of Science (JSPS) (K.F., 25109505) for research support. Portions of this research were carried out at the Stanford Synchrotron Radiation Lightsource (SSRL), a Directorate of SLAC National Accelerator Laboratory and an Office of Science User Facility operated for the U.S. Department of Energy (DOE) Office of Science by Stanford University. The SSRL Structural Molecular Biology Program is supported by the DOE Office of Biological and Environmental Research, and by the NIH, National Institute of General Medical Sciences (NIGMS) and the National Center for Research Resources (NCRR).

Notes and References

- (1). Solomon EI, Chen P, Metz M, Lee S-K, Palmer AE. *Angew. Chem. Int. Ed.* 2001; 40:4570–4590.
- (2). Solomon EI, Baldwin MJ, Lowery MD. *Chem. Rev.* 1992; 92:521–542.
- (3). Solomon EI, Sundaram UM, Machonkin TE. *Chem. Rev.* 1996; 96:2563–2606. [PubMed: 11848837]
- (4). Mirica LM, Ottenwaelder X, Stack TDP. *Chem. Rev.* 2004; 104:1013–1045. [PubMed: 14871148]
- (5). Lewis EA, Tolman WB. *Chem. Rev.* 2004; 104:1047–1076. [PubMed: 14871149]
- (6). Fukuzumi S, Karlin KD. *Coord. Chem. Rev.* 2013; 257:187–195. [PubMed: 23470920]
- (7). Ginsbach JW, Kieber-Emmons MT, Nomoto R, Noguchi A, Ohnishi Y, Solomon EI. *Proc. Natl. Acad. Sci. U.S.A.* 2012; 109:10793–10797. [PubMed: 22711806]
- (8). Hatcher LQ, Karlin KD. *J. Biol. Inorg. Chem.* 2004; 9:669–683. [PubMed: 15311336]
- (9). Jacobson RR, Tyeklár Z, Farooq A, Karlin KD, Liu S, Zubieta J. *J. Am. Chem. Soc.* 1988; 110:3690–3692.
- (10). Baldwin MJ, Ross PK, Pate JE, Tyeklár Z, Karlin KD, Solomon EI. *J. Am. Chem. Soc.* 1991; 113:8671–8679.

- (11). Schatz M, Becker M, Thaler F, Hampel F, Schindler S, Jacobson RR, Tyeklár Z, Murthy NN, Ghosh P, Chen Q, Zubieto J, Karlin KD. *Inorg. Chem.* 2001; 40:2312–2322. [PubMed: 11327908]
- (12). Zhang CX, Kaderli S, Costas M, Kim E-I, Neuhold Y-M, Karlin KD, Zuberbühler AD. *Inorg. Chem.* 2003; 42:1807–1824. [PubMed: 12639113]
- (13). A third end-on peroxy Cu(II)₂ species has also been observed.
- (14). Comba P. *Coord. Chem. Rev.* 2000; 200-202:217–245.
- (15). Park GY, Qayyum MF, Woertink J, Hodgson KO, Hedman B, Narducci Sarjeant AA, Solomon EI, Karlin KD. *J. Am. Chem. Soc.* 2012; 134:8513–8524. [PubMed: 22571744]
- (16). Que L, Tolman WB. *Angew. Chem. Int. Ed.* 2002; 41:1114–1137.
- (17). Kitajima N, Fujisawa K, Moro-oka Y, Toriumi K. *J. Am. Chem. Soc.* 1989; 111:8975–8976.
- (18). Kitajima N, Fujisawa K, Fujimoto C, Moro-oka Y, Hashimoto S, Kitagawa T, Toriumi K, Tatsumi K, Nakamura A. *J. Am. Chem. Soc.* 1992; 114:1277–1291.
- (19). Magnus KA, Hazes B, Ton-That H, Bonaventura C, Bonaventura J, Hol WG. *Proteins.* 1994; 19:302–309. [PubMed: 7984626]
- (20). Matoba Y, Kumagai T, Yamamoto A, Yoshitsu H, Sugiyama M. *J. Biol. Chem.* 2006; 281:8981–8990. [PubMed: 16436386]
- (21). Halfen JA, Mahapatra S, Wilkinson EC, Kaderli S, Young VG, Que L, Zuberbühler AD, Tolman WB. *Science.* 1996; 271:1397–1400. [PubMed: 8596910]
- (22). Mahapatra S, Halfen JA, Wilkinson EC, Pan G, Wang X, Young VG, Cramer CJ, Que LJ, Tolman WB. *J. Am. Chem. Soc.* 1996; 118:11555–11574.
- (23). Mahadevan V, Hou Z, Cole AP, Root DE, Lal TK, Solomon EI, Stack T. *J. Am. Chem. Soc.* 1997; 119:11996–11997.
- (24). Mirica LM, Vance M, Rudd DJ, Hedman B, Hodgson KO, Solomon EI, Stack TDP. *Science.* 2005; 308:1890–1892. [PubMed: 15976297]
- (25). Op't Holt BT, Vance MA, Mirica LM, Heppner DE, Stack TDP, Solomon EI. *J. Am. Chem. Soc.* 2009; 131:6421–6438. [PubMed: 19368383]
- (26). Nasir MS, Cohen BI, Karlin KD. *J. Am. Chem. Soc.* 1992; 114:2482–2494.
- (27). Karlin KD, Nasir MS, Cohen BI, Cruse RW, Kaderli S, Zuberbühler AD. *J. Am. Chem. Soc.* 1994; 116:1324–1336.
- (28). Pidcock E, Obias HV, Zhang CX, Karlin KD, Solomon EI. *J. Am. Chem. Soc.* 1998; 120:7841–7847.
- (29). Lam BM, Halfen JA, Young VG, Hagadorn JR, Holland PL, Lledós A, Cucurull-Sánchez L, Novoa JJ, Alvarez S, Tolman WB. *Inorg. Chem.* 2000; 39:4059–4072. [PubMed: 11198861]
- (30). DuBois JL, Mukherjee P, Collier AM, Mayer JM, Solomon EI, Hedman B, Stack TDP, Hodgson KO. *J. Am. Chem. Soc.* 1997; 119:8578–8579.
- (31). Szilagyi RK, Metz M, Solomon EI. *J. Phys. Chem. A.* 2002; 106:2994–3007.
- (32). Atanasov M, Comba P, Martin B, Müller V, Rajaraman G, Rohwer H, Wunderlich S. *J. Comput. Chem.* 2006; 27:1263–1277. [PubMed: 16786541]
- (33). This discussion of HF mixing needed in DFT calculations will be discussed further in another report.
- (34). Cruse RW, Kaderli S, Karlin KD. *J. Am. Chem. Soc.* 1988; 110:6882–6883.
- (35). Blackburn NJ, Strange RW, Farooq A, Haka MS, Karlin KD. *J. Am. Chem. Soc.* 1988; 110:4263–4272.
- (36). Cole AP, Mahadevan V, Mirica LM, Ottenwaelder X, Stack T. *Inorg. Chem.* 2005; 44:7345–7364. [PubMed: 16212361]
- (37). Tenderholt, AL.; Hedman, B.; Hodgson, KO. PySpline. Stanford Synchrotron Radiation Laboratory; Stanford CA: 2006.
- (38). Tenderholt A, Hedman B, Hodgson KO. *AIP Conf. Proc.* 2006; 882:105–107.
- (39). Frisch, MJ., et al. Gaussian 09 Revision A.1. Gaussian, Inc.; Wallingford CT: 2009.
- (40). Neese, F. ORCA: An ab initio, DFT, and semiempirical electronic structure package, Version 2.6 revision 35. Universität Bonn; Bonn—Germany: 2008.

- (41). Becke AD. Phys. Rev. A. 1988; 83:3098–3100. [PubMed: 9900728]
- (42). Perdew J. Phys. Rev. B. 1986; 33:8822–8824.
- (43). Lee C, Yang W, Parr RG. Phys. Rev. B. 1988; 37:785–789.
- (44). Miehlich B, Savin A, Stoll H, Preuss H. Chem. Phys. Lett. 1989; 157:200–206.
- (45). BLYP gives very similar results as BP86.
- (46). Becke AD. J. Chem. Phys. 1993; 98:5648–5652.
- (47). Karlin KD, Hayes JC, Gultneh Y, Cruse RW, McKown JW, Hutchinson JP, Zubieta J. J. Am. Chem. Soc. 1984; 106:2121–2128.
- (48). Merrick JP, Moran D, Radom L. J. Phys. Chem. A. 2007; 111:11683–11700. [PubMed: 17948971]
- (49). <http://cccbdb.nist.gov/vibscalejust.asp>
- (50). Tomasi J, Mennucci B, Cammi R. Chem. Rev. 2005; 105:2999–3094. [PubMed: 16092826]
- (51). Grimme S, Antony J, Ehrlich S, Krieg H. J. Chem. Phys. 2010; 132:154104–154119. [PubMed: 20423165]
- (52). Jansen G, Hess BA. Phys. Rev. A. 2011; 39:6016–6017. [PubMed: 9901188]
- (53). Tenderholt, AL. QMForge, v. 2.1. Stanford University; Stanford CA: 2007. <http://qmforge.sourceforge.net>
- (54). Mulliken R. J. Chem. Phys. 1955; 23:1833–1840.
- (55). Mayer I. Chem. Phys. Lett. 1983; 97:270–274.
- (56). Bridgeman AJ, Cavigliasso G, Ireland LR, Rothery J. J. Chem. Soc., Dalton Trans. 2001:2095–2108.
- (57). Humphrey W, Dalke A, Schulten K. J. Mol. Graphics. 1996; 14:33–38.
- (58). Yamaguchi K, Jensen F, Dorigo A, Houk KN. Chem. Phys. Lett. 1988; 149:537–542.
- (59). Kitagawa Y, Saito T, Ito M, Nakanishi Y, Shoji M, Koizumi K, Yamanaka S, Kawakami T, Okumura M, Yamaguchi K. Int. J. Quantum Chem. 2007; 107:3094–3102.
- (60). For example, the BS spin expectation value for species **A** ($C-O = 2.80 \text{ \AA}$) is 0.87 (Table 7) with contamination from only the $S_T = 1$ excited state. Thus, equation 1 is used for energy correction. At the TS, the BS spin expectation value is 1.10 (Table 7) with spin contamination from the $S_T = 1$ and $S_T = 2$ excited states. An average spin expectation of 0.83 (average of the spin expectation values from species **A** to **F**, Table S11) was used as the spin contamination from the $S_T = 1$ state at the TS with the rest from the $S_T = 2$ state.
- (61). de Groot FMF. Physica B. 1995; 208-209:15–18.
- (62). Fuggle JC, Alvarado SF. Phys. Rev. A. 1980; 22:1615–1624.
- (63). George SJ, Lowery MD, Solomon EI, Cramer SP. J. Am. Chem. Soc. 1993; 115:2968–2969.
- (64). Sarangi R, Abobeella N, Fujisawa K, Tolman WB, Hedman B, Hodgson KO, Solomon EI. J. Am. Chem. Soc. 2006; 128:8286–8296. [PubMed: 16787093]
- (65). DeBeer George S, Metz M, Szilagyi RK, Wang H, Cramer SP, Lu Y, Tolman WB, Hedman B, Hodgson KO, Solomon EI. J. Am. Chem. Soc. 2001; 123:5757–5767. [PubMed: 11403610]
- (66). High covalency can lead to shake-up satellite features on the L-edge which redistribute the intensity (*vide infra*), and therefore, total integrated intensities for **1** and **2** were used for comparison to square planar $[\text{CuCl}_4]^{2-}$.
- (67). Solomon EI, Szilagyi RK, DeBeer George S, Basumallick L. Chem. Rev. 2004; 104:419–458. [PubMed: 14871131]
- (68). Chen P, Root DE, Campochiaro C, Fujisawa K, Solomon EI. J. Am. Chem. Soc. 2003; 125:466–474. [PubMed: 12517160]
- (69). Mizuno M, Hayashi H, Fujinami S, Furutachi H, Nagatomo S, Otake S, Uozumi K, Suzuki M, Kitagawa T. Inorg. Chem. 2003; 42:8534–8544. [PubMed: 14658910]
- (70). Abobeella NW, Lewis EA, Reynolds AM, Brennessel WW, Cramer CJ, Tolman WB. J. Am. Chem. Soc. 2002; 124:10660–10661. [PubMed: 12207513]
- (71). Hayashi H, Fujinami S, Nagatomo S, Ogo S, Suzuki M, Uehara A, Watanabe Y, Kitagawa T. J. Am. Chem. Soc. 2000; 122:2124–2125.

- (72). Mahapatra S, Young VG, Kaderli S, Zuberbühler AD, Tolman WB. *Angew. Chem. Int. Ed.* 1997; 36:130–133.
- (73). Straub BF, Rominger F, Hofmann P. *Chem. Commun.* 2000:1611–1612.
- (74). Zhou L, Powell D, Nicholas KM. *Inorg. Chem.* 2006; 45:3840–3842. [PubMed: 16676937]
- (75). Henson MJ, Mukherjee P, Root DE, Stack TDP, Solomon EI. *J. Am. Chem. Soc.* 1999; 121:10332–10345.
- (76). DFT calculations with B3LYP and the all-electron TZVP/SVP basis set generally overestimate the O-O stretching frequency in side-on peroxy Cu(II)₂ species by ~100 cm⁻¹. In the $\text{P}^{\text{NO}_2-\text{XYL}}$ complex, the frequency is overestimated by 132 cm⁻¹. This likely reflects an overestimation of the bend of the Cu₂O₂ dihedral angle, which has previously been shown in ref 77 to increase the O-O stretching frequency.
- (77). Pidcock E, Obias HV, Abe M, Liang H-C, Karlin KD, Solomon EI. *J. Am. Chem. Soc.* 1999; 121:1299–1308.
- (78). Based on the available crystal structure of $[\text{Cu}(\text{II})_2(\text{H-XYL-O}^-)(\text{OH}^-)]^{2+}$.
- (79). Siegbahn PEM, Blomberg MRA, Chen S-L. *J. Chem. Theory Comput.* 2010; 6:2040–2044.
- (80). The reaction coordinates obtained with and without dispersion and relativistic effects are similar. The electronic structures of 1 and 2 also do not change significantly when dispersion and relativistic effects are added.
- (81). Karlin KD, Kaderli S, Zuberbühler AD. *Acc. Chem. Res.* 1997; 30:139–147.
- (82). The calculated ΔE^\ddagger with 10 percent HF added, instead of 20 percent HF, is 23 kcal/mol, which is reduced to 13 kcal/mol when dispersion and relativistic effects are included.
- (83). NIH shift experimentally observed with a methyl substituted at the C12 position (Figure 7) is calculated to take place after the TS and therefore does not affect the TS.
- (84). The C-O MBO in a fully optimized molecule of NO₂-phenolate and NO₂-phenol (without any Cu) are 1.807 and 1.233, respectively.
- (85). There is a slight increase in charge and spin on the Cu centers that is due to approximately 11 percent α and β electron donation (2 percent α , 9 percent β from Cu₁ and 9 percent α , 3 percent β from Cu₂) from the coppers to the peroxy moiety (Table 8).
- (86). At point G the peroxy π^* and σ^* orbitals are hybridized (Figure S2, orbitals 197 and 198). The peroxy σ^* (orbital 210 in Figure S2 A) is lowerd in energy relative to the peroxy π_{σ}^* (LUMO, 197) at point G. For a planar Cu₂O₂ core, the peroxy π_{σ}^* HOMO is in the plane and σ antibonding to Cu, whereas the π_{ν}^* is out of the Cu₂O₂ plane and non-bonding to Cu. In the xylyl system, the peroxy π_{σ}^* and π_{ν}^* orbitals hybridize because the Cu₂O₂ core is butterflyed.
- (87). The diradical formation is due to the peroxy π^* and σ^* orbitals hybridizing to maximize overlap with the π cloud of the substrate HOMO and resulting in greater overlap with the peroxy β LUMO compared to the peroxy α LUMO (Figure S3, point Y).
- (88). Similar results are obtained with a five coordinate Cu system, $[\text{Cu}(\text{II})_2(\text{NH}_3)_6(\text{O}_2^{2-})]^{2+}$, instead of a four coordinate Cu species and with NO₂ substituted at the para position of the benzene.
- (89). At the TS (Table S15, point Y), the Mülliken spins on the Cu centers decrease. However, the Mülliken charges (Table S14) also decrease showing that the Cu centers are not oxidized to Cu(III)'s.
- (90). Synthetic modifications designed to experimentally probe for or induce radical intermediates, along with computational studies, are planned for future investigations.
- (91). Similar results are obtained with water as the exogenous base.
- (92). Winkler ME, Lerch K, Solomon EI. *J. Am. Chem. Soc.* 1981; 103:7001–7003.
- (93). Wilcox DE, Porras AG, Hwang YT, Lerch K, Winkler ME, Solomon EI. *J. Am. Chem. Soc.* 1985; 107:4015–4027.

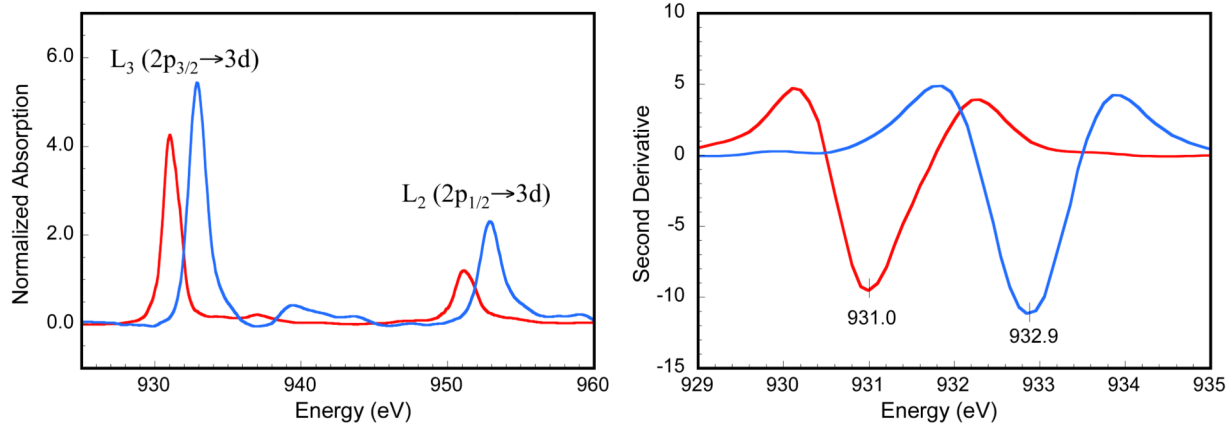


Figure 1.

Cu L-edge XAS spectra of **1** (red line) and **2** (blue line). (Left) Normalized Cu L-edge XAS spectra. The weak edge jumps were simulated with arctangent functions and subtracted from the entire spectrum. The intense peaks at ~930 and ~950 eV represent the L₃-edge ($2p_{3/2} \rightarrow 3d$ transition) and the L₂-edge ($2p_{1/2} \rightarrow 3d$ transition), respectively. (Right) Smoothed second derivative of the Cu L₃-edge region.

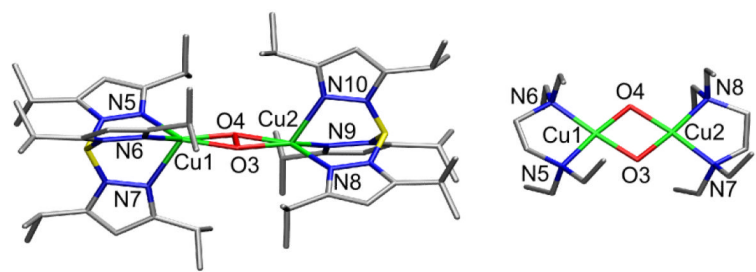


Figure 2.

Schematic representations of (left) **1** and (right) **2**. H atoms are omitted for clarity.

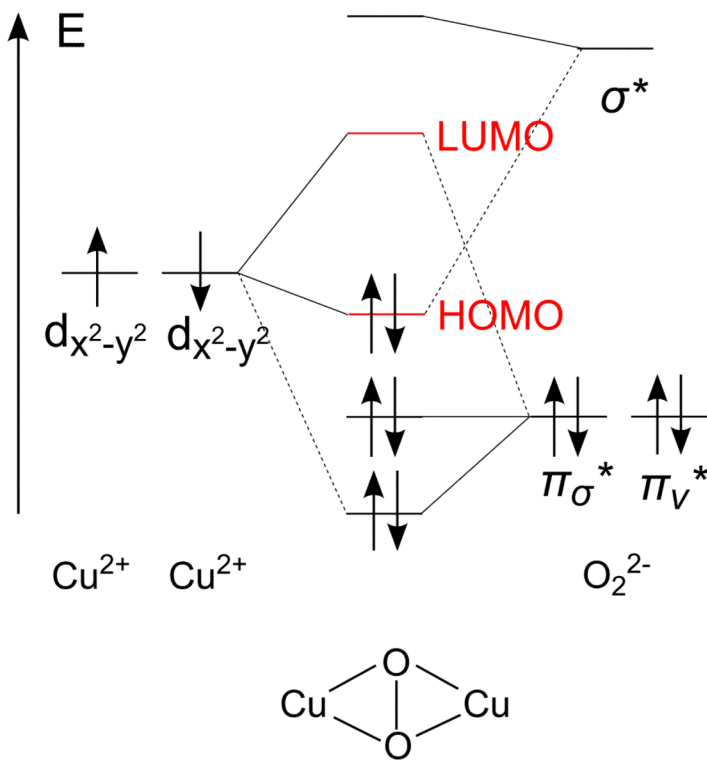
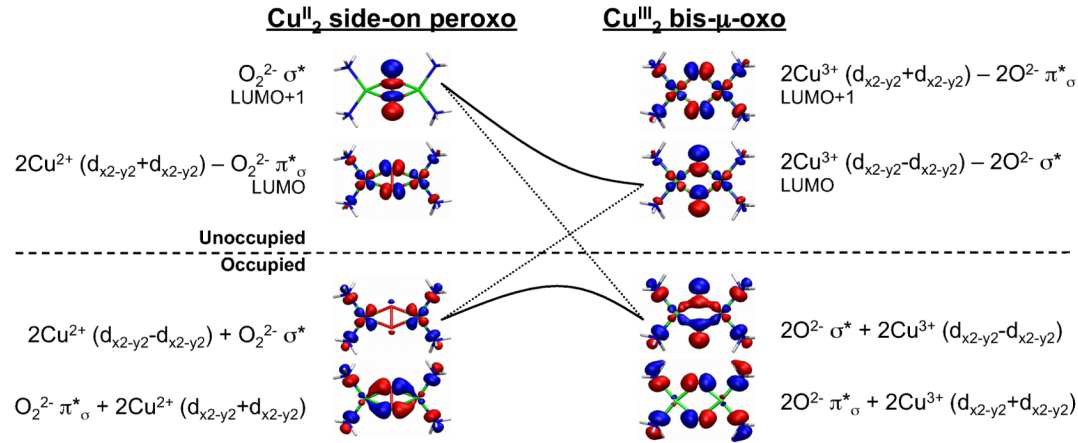


Figure 3.
Schematic molecular orbital diagram for **P** species.

**Figure 4.**

The two key unoccupied MOs and their occupied counterparts in **P** and **O**. The σ^* orbital in **P** has small backbonding from a occupied Cu $d_{x^2-y^2}$ orbital that is not shown here.

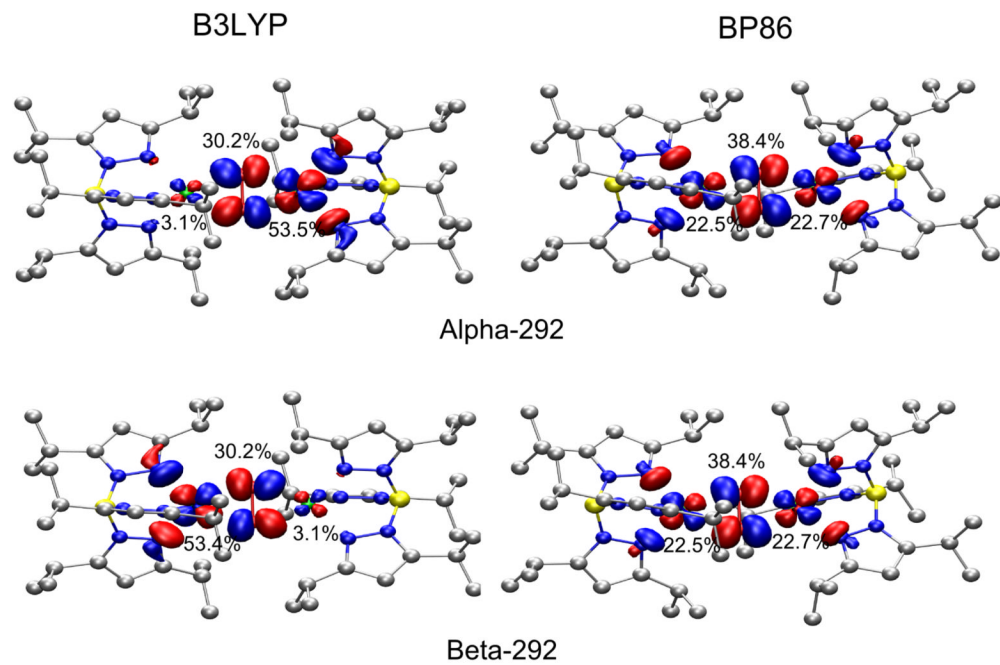


Figure 5.

Isosurface plots (isovalue 0.04 au) of α and β LUMO of **1** from B3LYP in the BS ($M_S = 0$) state (left) and BP86 (right) spin-unrestricted calculations.

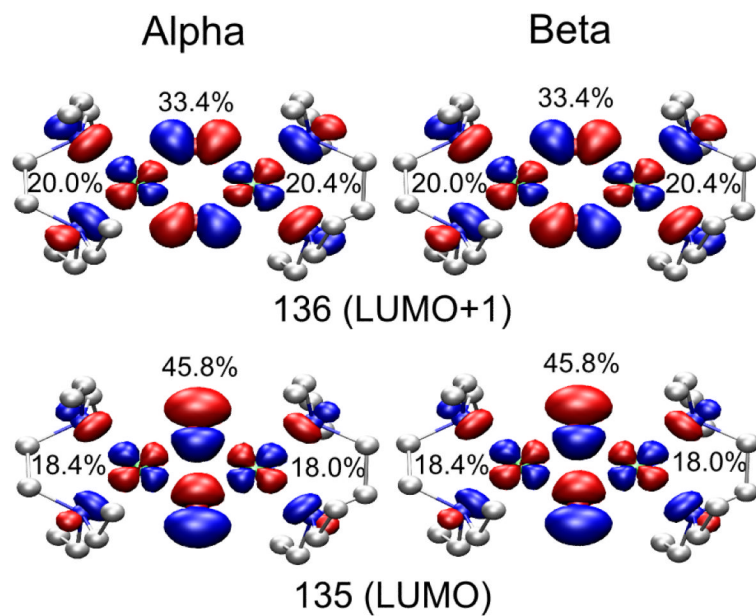
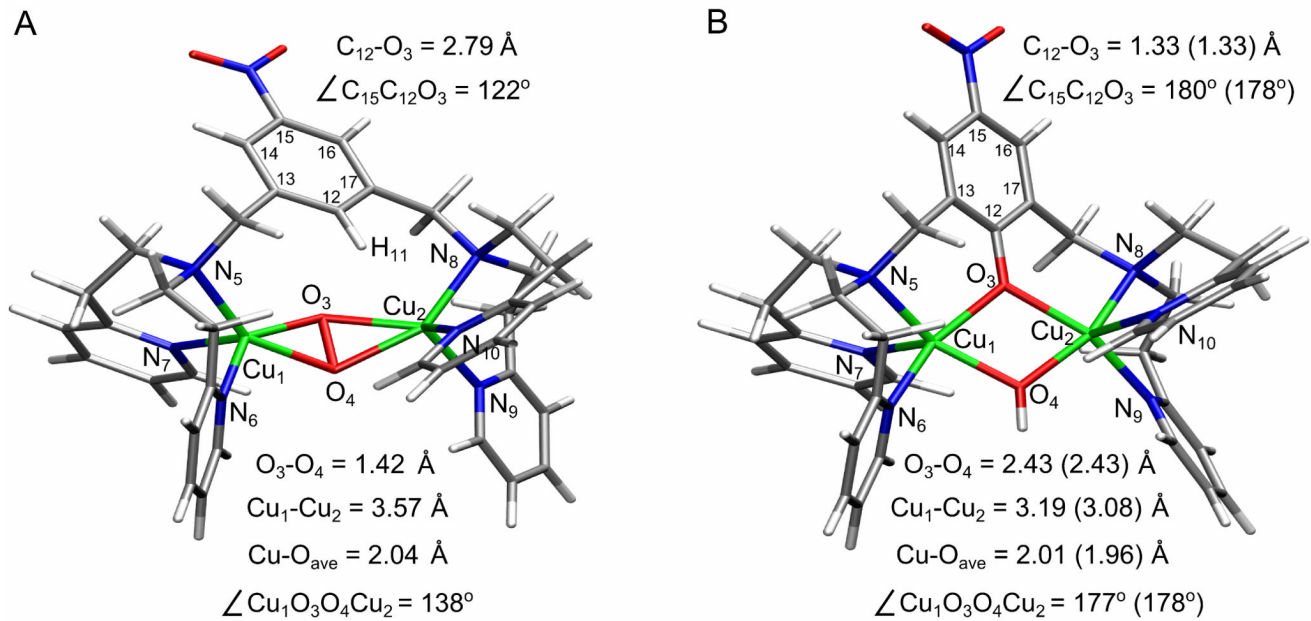
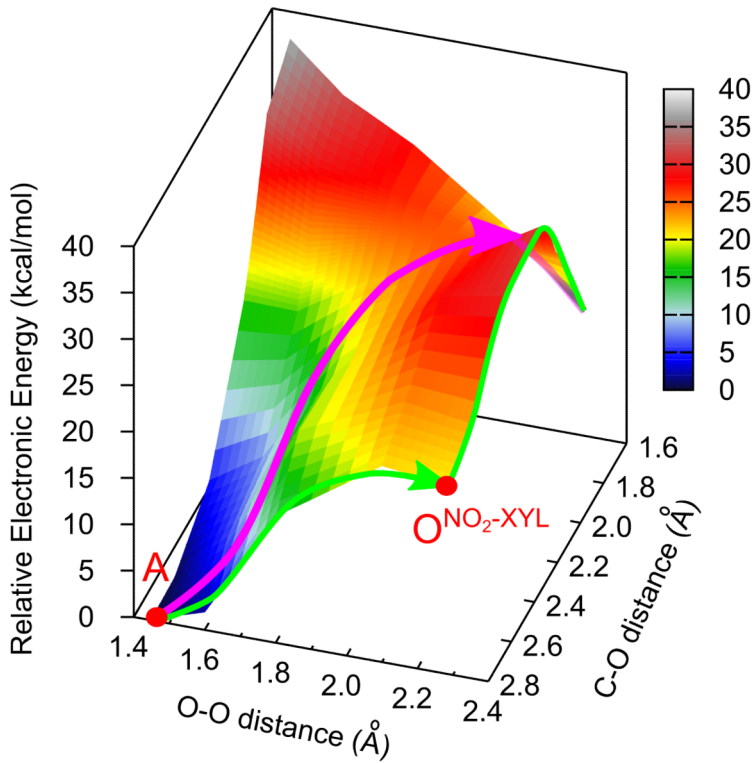


Figure 6.

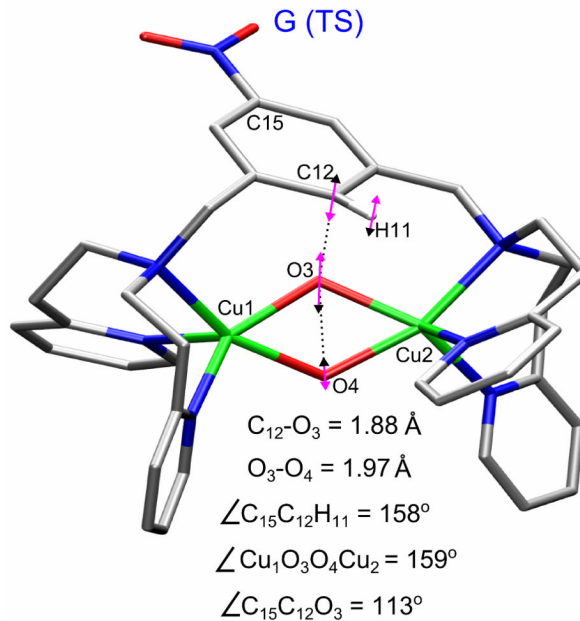
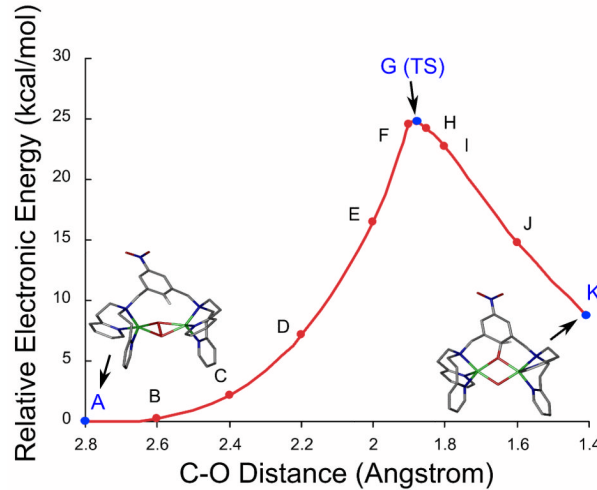
Isosurface plots (isovalue 0.04 au) of α, β LUMO and LUMO+1 of **2** from 38% HF spin-unrestricted calculations.

**Figure 7.**

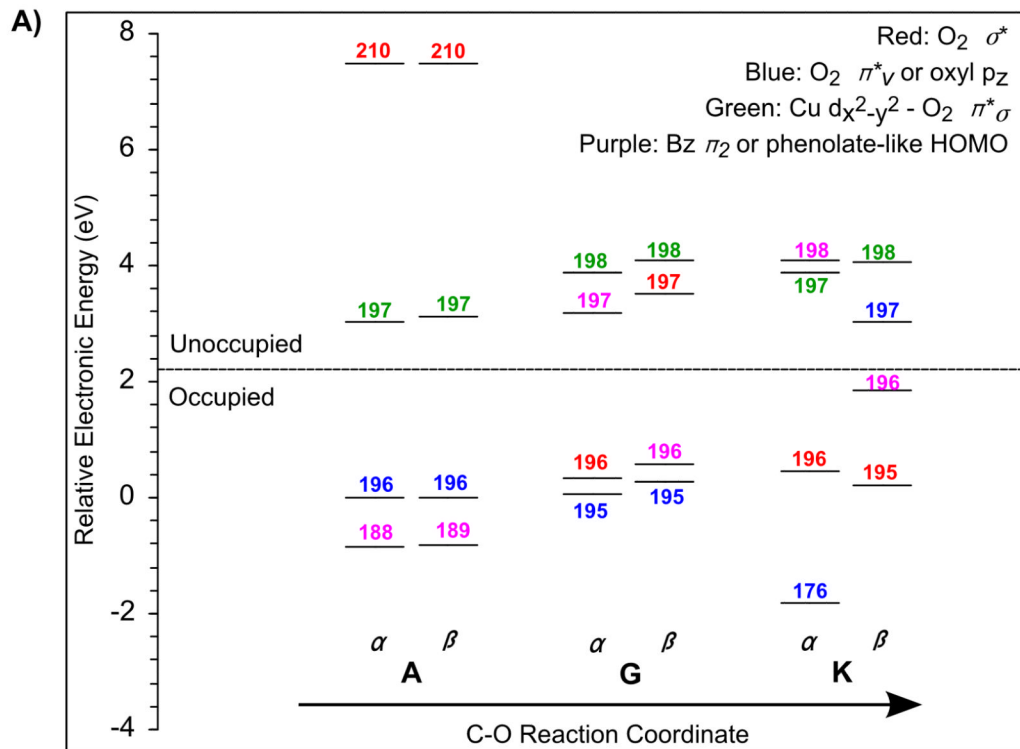
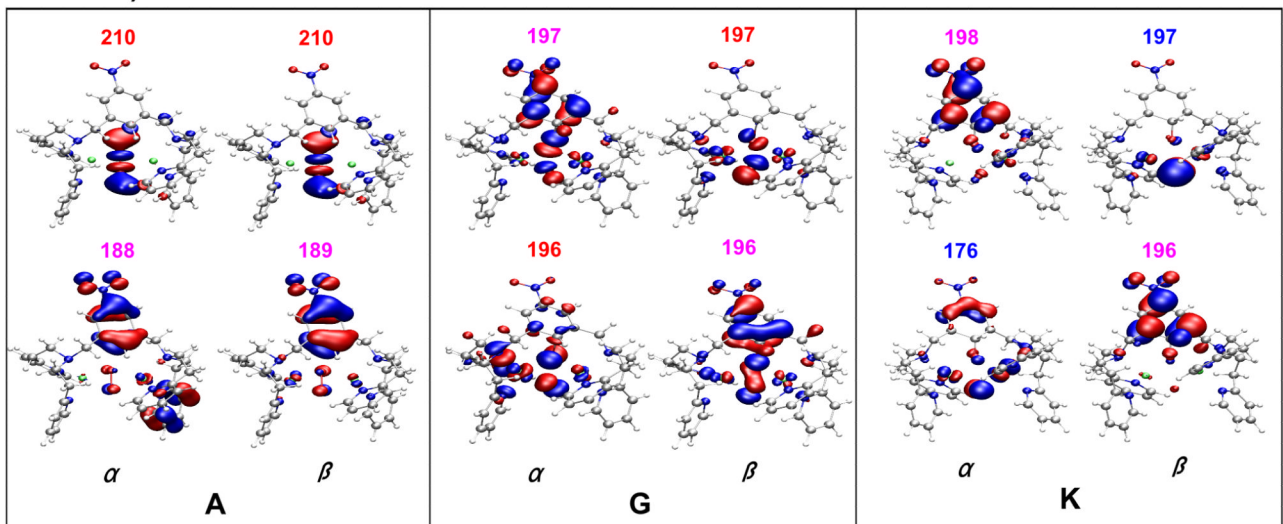
B3LYP optimized structures of A) the P^{NO_2-XYL} complex, and B) the final hydroxylated product $[Cu(II)_2(NO_2-XYL-O^-)(OH^-)]^{2+}$. Crystallographic parameters are given in parentheses.

**Figure 8.**

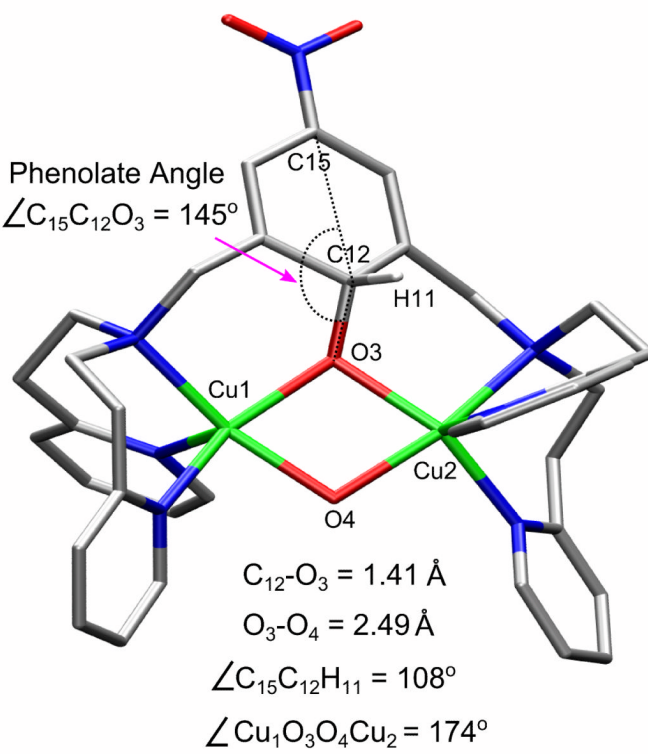
2-D potential energy surface (PES) showing electronic energy changes as a function of O_3-O_4 and $C_{12}-O_3$ distances for $[Cu(II)_2(NO_2-XYL)(O_2)]^{2+}$. The pink line indicates the lowest energy route on the PES from A, the 2.80 Å $C_{12}-O_3$ P^{NO_2-XYL} starting structure, leading to K, the end species (not shown here). The green line indicates the path taken to first form O^{NO_2-XYL} followed by $C_{12}-O_3$ bond formation.

**Figure 9.**

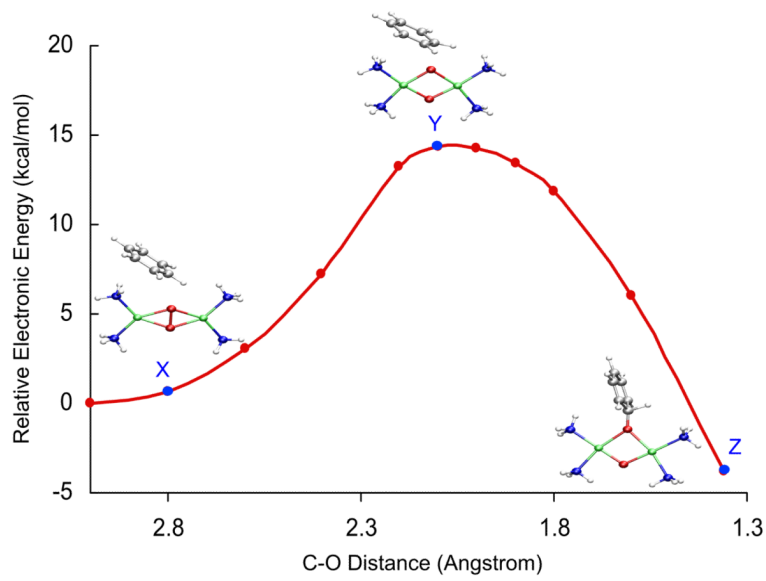
(Top) Potential energy surface of the formation of phenolate along the $C_{12}-O_3$ coordinate for $[Cu(II)_2(NO-XYL)(O_2)]^{2+}$ extracted from the lowest energy path of the 2-D PES (Figure 8, pink line) along O_3-O_4 and $C_{12}-O_3$ distances with additional points added near the transition state (TS) and at the end point K. All hydrogens except H_{11} are omitted for clarity. (Bottom) Transition state structure for $C_{12}-O_3$ bond formation. The pink arrows represent the mode of the imaginary frequency of -547 cm^{-1} with the length of the arrows representing the relative displacement of the atoms.

**B)****Figure 10.**

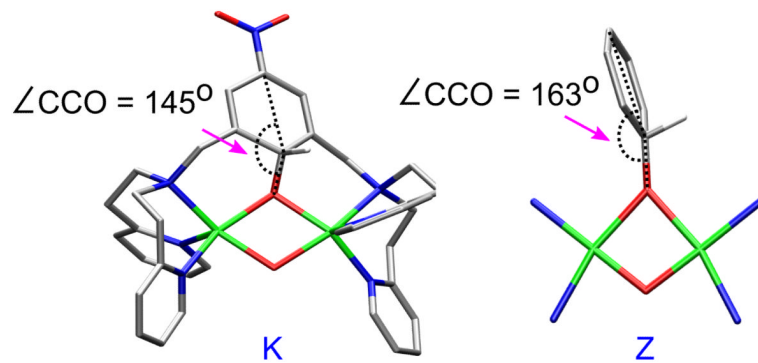
Key orbitals along the $C_{12}-O_3$ reaction coordinate for $[Cu(II)_2(NO_2-XYL)(O_2)]^{2+}$. The unoccupied peroxy σ^* orbitals ($210\alpha, \beta$ in **A**) are lowered in energy along the coordinate. An α electron is donated from the occupied xylyl HOMO (orbital 188 in **A**) to the peroxy σ^* orbital leaving an α hole on the xylyl (orbital 198α in **K**). The β hole ends up on the distal O_4 (oxy p_z -like orbital, 197β in **K**; the z-axis is perpendicular to the Cu_2O_2 plane).

**Figure 11.**

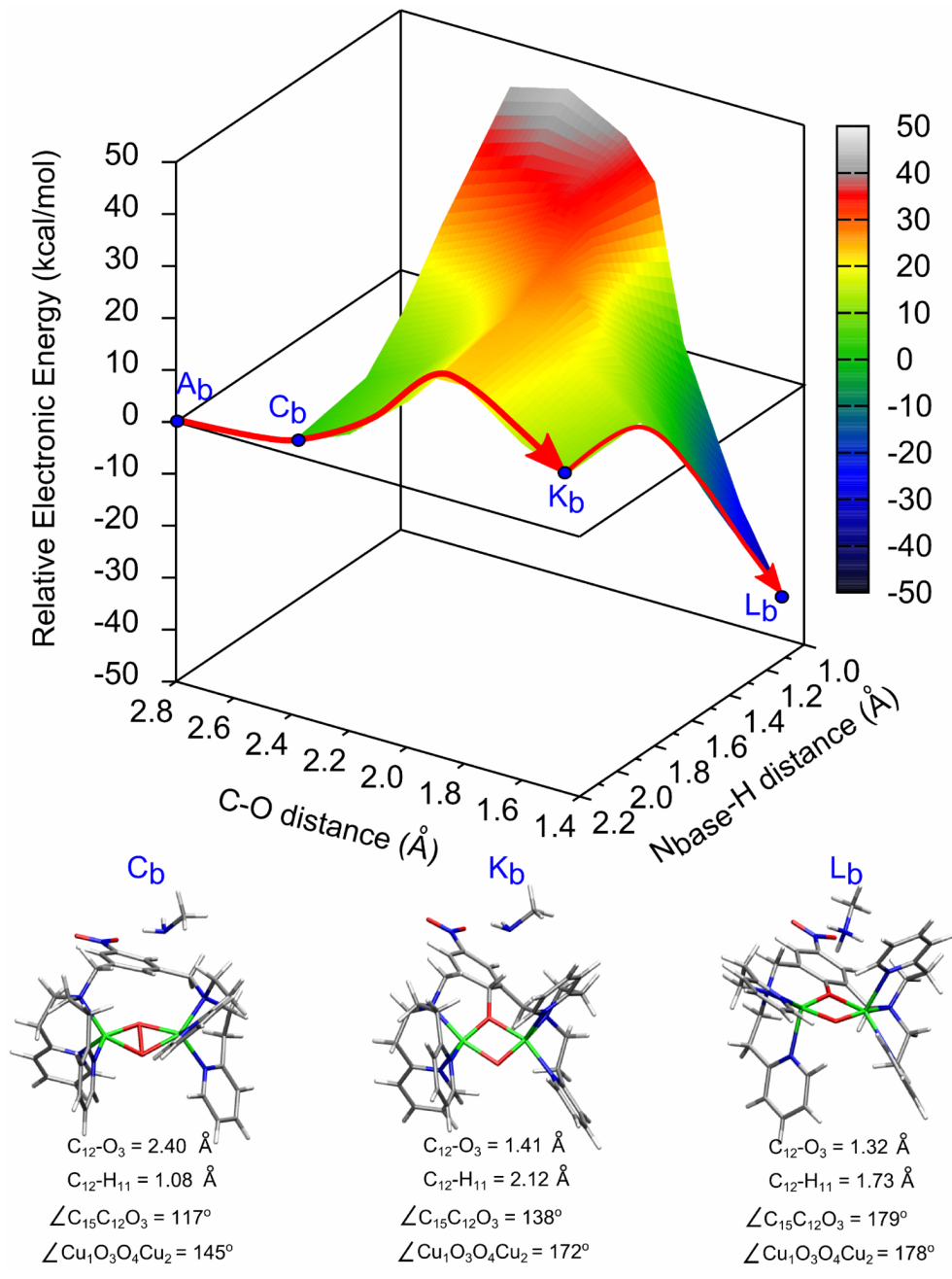
Structure of species **K**. All hydrogens except H₁₁ are omitted for clarity.

**Figure 12.**

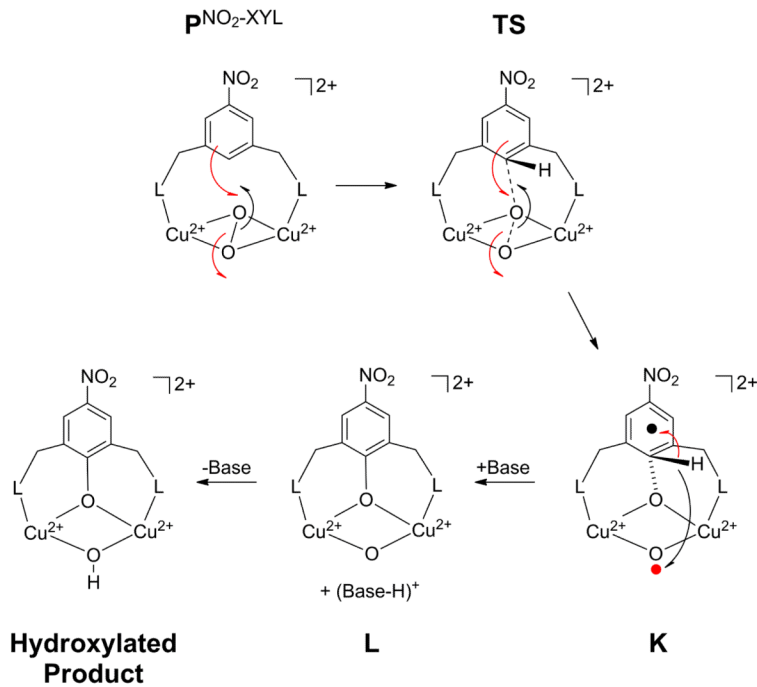
Potential energy surface for the EAS reaction of benzene with $[\text{Cu}(\text{II})_2(\text{NH}_3)_4(\text{O}_2^{2-})]^{2+}$.

**Figure 13.**

Structures of species **K** versus **Z** formed at the end of the EAS reaction coordinates for $[\text{Cu(II)}_2(\text{NO}_2\text{-XYL})(\text{O}_2)]^{2+}$ and $[\text{Cu(II)}_2(\text{NH}_3)_4(\text{O}_2^{2-})]^{2+}$, respectively, but before *ortho*- H^+ cleavage. All hydrogens except *ortho*- H are omitted for clarity.

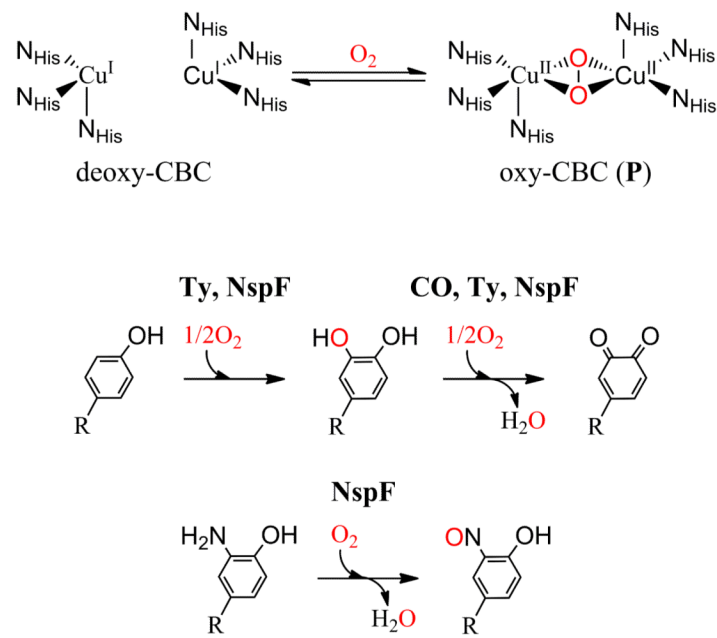
**Figure 14.**

2-D potential energy surface (PES) for $[\text{Cu(II)}_2(\text{NO}_2\text{-XYL})(\text{O}_2)]^{2+}$ showing electronic energy changes as a function of $\text{C}_{12}\text{-O}_3$ and $\text{N}_{\text{base}}\text{-H}_{11}$ distances with methylamine as the base. The red line indicates the lowest energy route on the PES starting from A_b through C_b to K_b and finally forming the deprotonated species L_b . L_b is ~ 41 kcal/mol lower in energy than A_b .

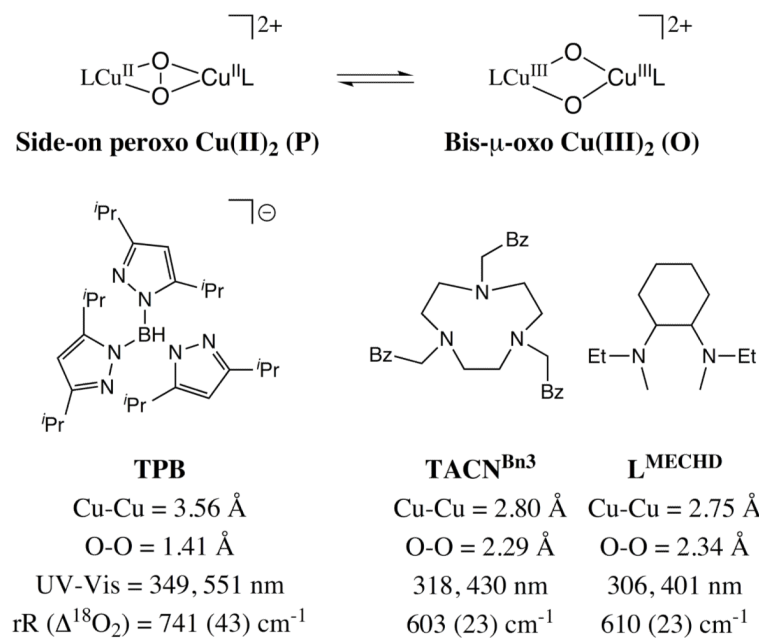
**Figure 15.**

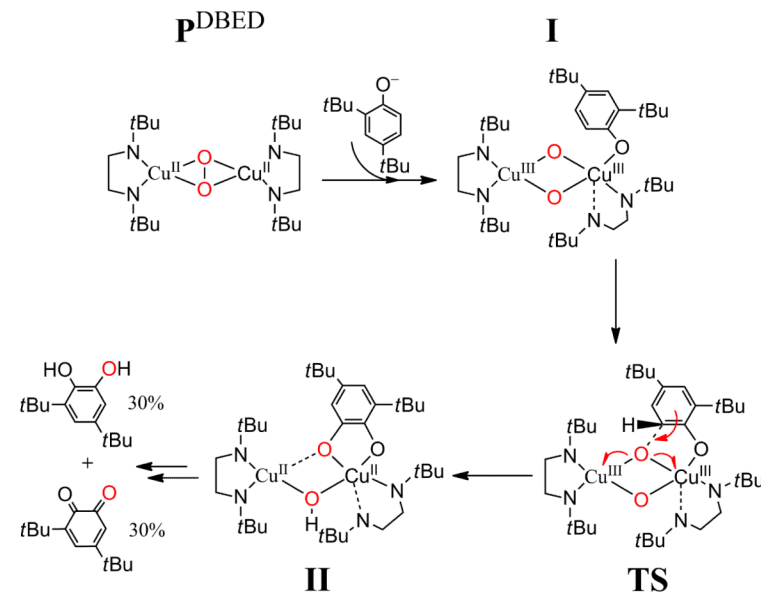
Schematic mechanism of aromatic hydroxylation performed by **P^{NO₂-XYL}** in $[\text{Cu(II)}_2(\text{NO}_2\text{-XYL})(\text{O}_2)]^{2+}$. The red and black arrows represent transfer of α and β electrons, respectively. In going through the transition state (**TS**) to **K**, a pair of α and β electrons are transferred from the xylyl ring and peroxy π^* orbital, respectively, to concertedly form the C-O bond and cleave the O-O bond. This produces an α spin on O_d that is paired with the β radical on the ring. In proceeding from **K** to **L** and subsequently to the hydroxylated product, the $\alpha\text{-H}^+$ is transferred to the O_d via a base. As the $\alpha\text{-C-H}$ bond is cleaved, its α and β electrons are transferred to the phenolate and O_d, respectively, leading to the full formation of the phenolate C-O bond.

Coupled Binuclear Copper (CBC) Proteins: Hc, CO, Ty, NspF

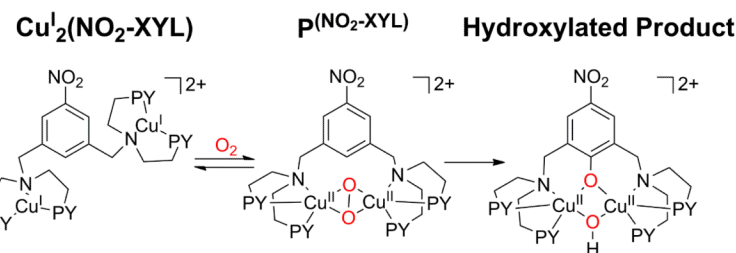


Scheme 1.

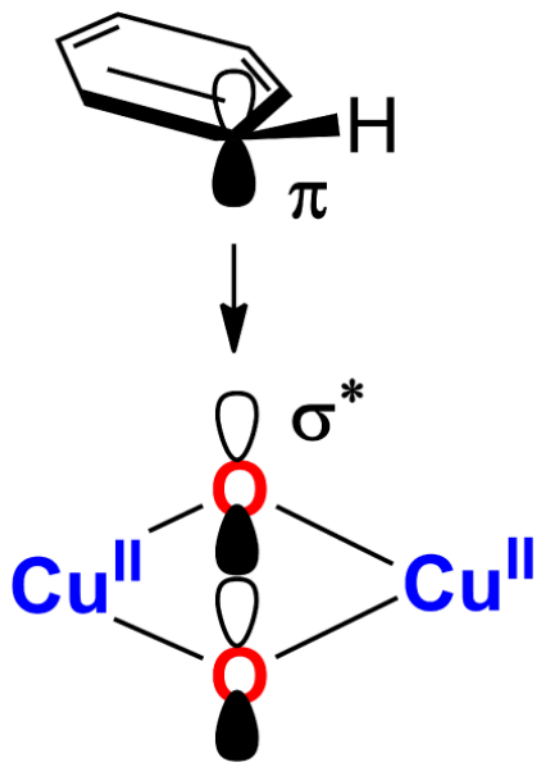
**Scheme 2.**



Scheme 3.



Scheme 4.



Scheme 5.

Table 1Cu L-Edge X-ray Absorption Edge Energies (eV) and Cu Character in Ψ^*_{LUMO} of **1** and **2**.

	2p → 3d Energy ^a			Cu Character in Ψ^*_{LUMO}
	L ₃ -edge	L ₂ -edge	(% Hole)	
1	931.0	951.0	52 ± 4	
2 ^b	932.9	952.8	79 ± 6	

^aEnergy resolution is ~0.1 eV. The energy is determined from the minimum intensity of the second derivative.

^bTwo-hole system (see text for detail).

Table 2

Comparison of Select Structural Parameters of **1** from DFT Calculations and Crystallography. All Bond Lengths are in Å.

Parameter	X-ray ¹⁸	BP86	10% HF	B3LYP	38% HF
∠Cu1,O3,O4,Cu2 ^a	180.0	174.6	179.8	180.0	179.8
O3-O4	1.413	1.450	1.446	1.457	1.484
Cu1-Cu2	3.556	3.705	3.728	3.718	3.681
Ave Cu-O	1.914	1.993	1.999	1.997	1.985
Ave Cu-Neq	1.997	2.007	2.022	2.035	2.058
Ave Cu-Nax	2.260	2.244	2.283	2.300	2.322

^aDihedral angle of the Cu₂O₂ core

Table 3

Comparison of Select Structural Parameters of **2** from DFT Calculations and Crystallography. All Bond Lengths are in Å.

Parameter	X-ray ²³	BP86	10% HF	B3LYP	38% HF
∠Cu1,O3,O4,Cu2 ^a	173.7	180.0	180.0	180.0	180.0
O3-O4	2.344	2.372	2.363	2.349	2.329
Cu1-Cu2 ^b	2.748	2.797	2.781	2.775	2.755
Ave Cu-O ^b	1.808	1.834	1.825	1.818	1.804
Ave Cu-N ^b	1.938	2.006	2.008	2.009	2.010

^aDihedral angle of the Cu₂O₂ core

^bEXAFS data of **2** (Cu···Cu = 2.75 Å, Cu-O = 1.80 Å, Cu-N = 1.92 Å)³⁰

Table 4

Per Cu Mülliken Population in the α Plus β Unoccupied Orbitals from Spin-Unrestricted Calculations of **1** and **2**. Spin Expectation Values Given in Parenthesis.

Functional	1 (LUMO)	2 (LUMO & LUMO+1)^a
BP86	45 (0.00)	66 (0.00)
10% HF	49 (0.45)	68 (0.00)
B3LYP	57 (0.61)	71 (0.00)
38% HF	70 (0.90)	76 (0.00)

^aNumbers reported here are for two holes per 3d⁸ Cu(III).

Table 5

Distances and Mayer Bond Order (MBO) for C₁₂–O₃ and O₃–O₄ along the C₁₂–O₃ Coordinate for [Cu(II)₂(NO₂-XYL)(O₂)]²⁺.

Structure	C ₁₂ –O ₃ Å	C ₁₂ –O ₃ MBO	O ₃ –O ₄ MBO	CO Formed %	OO Formed %
A	2.800	<0.01	0.733		100
B	2.600	<0.01	0.723		99
C	2.400	<0.01	0.709		97
D	2.200	<0.01	0.688		94
E	2.000	<0.01	0.635		87
F	1.900	0.030	0.572	3	78
G (TS)^a	1.880	0.296	0.272	25	37
H	1.850	0.426	0.133	36	18
I	1.800	0.511	0.095	43	13
J	1.600	0.730	0.035	62	5
K^a	1.409	0.893	<0.01	76	
L^b	1.303	1.180	<0.01	100	

^aFully optimized structures with no constraints.

^bOptimized structure with C₁₂–H₁₁ broken and H⁺ removed.

Table 6Mulliken Charge of Key Species along the C₁₂–O₃ Coordinate for [Cu(II)₂(NO₂-XYL)(O₂)]²⁺.

	2.80 A	1.88 G (TS) ^a	1.409 K ^a
Cu ₁	0.38	0.41	0.40
Cu ₂	0.37	0.44	0.42
O ₃	-0.25	-0.42	-0.48
O ₄	-0.23	-0.35	-0.31
(NO ₂ -C ₆ H ₂)	-0.05	0.13	0.06
H ₁₁	0.07	0.12	0.12
rest	1.78	1.80	1.90

^aFully optimized structures with no constraints.

Table 7

Mülliken Spin and Spin Expectation of Key Species along the C₁₂–O₃ Coordinate for [Cu(II)₂(NO₂-XYL)(O₂)]²⁺.

	2.80 A	1.88 G (TS) ^a	1.409 K ^a
Cu ₁	0.44	0.52	0.59
Cu ₂	-0.44	-0.52	-0.57
O ₃	0.02	-0.21	-0.03
O ₄	-0.01	0.52	0.96
(NO ₂ -C ₆ H ₂)	0.00	-0.31	-0.98
H ₁₁	0.00	0.02	-0.07
rest	-0.01	-0.01	0.03
<S ² >	0.87	1.10	1.95

^aFully optimized TS and K end species with no constraints.

Table 8

Change in Mülliken Population of the Filled Orbitals along the C₁₂–O₃ Coordinate Compared to Structure A.
All Numbers are in % of an electron.

	G (1.88)		K (1.409)	
	α	β	α	β
Cu ₁ (d orbitals)	-2	-9	1	-16
Cu ₂ (d orbitals)	-9	-3	-13	-3
O ₃ (p orbitals)	0	24	16	22
O ₄ (p orbitals)	34	-17	50	-41
(NO ₂ -C ₆ H ₃)	-23	5	-54	38